Solar-sail transfers to Earth-Moon L2-displaced vertical Lyapunov orbits

Technische Universiteit Delft

TU Delft

Master Thesis

T.D. van den Oever

Front cover image taken from:
https://moon.nasa.gov/resources/127/lunar-near-side/?category=images

Solar-sail transfers to Earth-Moon L2-displaced vertical Lyapunov orbits

Master Thesis

by

T.D. van den Oever

to obtain the degree of Master of Science
at the Delft University of Technology,
to be defended publicly on Monday August 27, 2018 at 13:00 AM.

Student number:	4145704	
Supervisor:	Dr. M. J. Heiligers	
Thesis Committee:	Prof. P. N. A. M. Visser	Committee chair
	Dr. M. J. Heiligers	Supervisor
	Dr. R. Fonod	External examinator

An electronic version of this thesis is available at http://repository.tudelft.nl/.

TU Delft

Preface

When I was five years old, I gave my first class lecture about the Solar System. I brought two footballs to the class and explained how the Earth rotates around the Sun. Since then, my fascination for spaceflight has only grown. The completion of this thesis concludes my time at Faculty of Aerospace Engineering of the University of Technology Delft, fulfilling a long held dream.

Although I always knew I wanted to complete a spaceflight master, I had no idea in what direction I wanted to specialize. During my minor at the Iowa State University, I took an course on astrodynamics and I was soon captured by the mathematical beauty of the motion of bodies in the Solar System. This led to the decision to follow the space exploration track and took an odd combination of courses in astrodynamics, spacecraft instrumentation and aircraft trajectory optimization. During my masters I came into contact with my supervisor Jeannette Heiligers, who offered me an internship at the Colorado Center for Astrodynamic Research. The internship assignment was to optimize spacecraft trajectories for planetary pole-sitters, which can be used to perform polar observations at Venus, Earth and Mars. The odd combination of courses was actually pretty handy for this project. After a successful and fun internship period in Colorado, she offered me this master thesis project in Delft.

Completing this thesis would not have been without others. First, I would like to thank my parents for their continuous and unconditional support throughout my studies. Also, I would like to thank my hard-working little sister, who grew to be a source of inspiration for me over the last years.

My friends gave me an amazing time in Delft and also helped me through a more challenging phase as well. Special acknowledgements to my friends of room 2.56, our motto now applies to me as well. I want to thank Carolien, who was initially a sparring partner during our daily elevator commute, but now also proofreads my thesis and takes me on city trips.

Finally, I would like to thank my supervisor Jeannette Heiligers for her support and advice, both during the internship in Colorado and the master thesis in Delft. You enabled me to work on challenging and fun problems in trajectory optimization and design. Your thorough feedback brought my academic reporting skills to a whole new level. I couldn't have wished for a more dedicated supervisor.

Tom van den Oever
Delft, July 2018

Executive Summary

The purpose of this thesis is to find solar-sail transfer trajectories to a constellation of solar-sail displaced L_2 vertical Lyapunov orbits in the Earth-Moon system, to support communication with the far side of the Moon and the lunar South Pole. The far side of the Moon is scientifically interesting as it includes the Aitken Basin which reveals deeper layers of the lunar crust. The lunar South Pole is considered a possible location for a future human base, as it provides access to continuous solar power and possibly water ice in permanently shadowed craters. For proposed missions to the far side of the Moon or the human base at the lunar South Pole, a communication link with Earth will be required.

Spacecraft in natural L_2 halo orbits have been considered for lunar farside coverage, but cannot guarantee continuous coverage of the lunar South Pole. By utilizing a solar sail, new types of orbits can be found with a coverage optimized for a specific region. Solar sails generate a small but continuous control force by reflecting and absorbing photons. This control force can be utilized to steer a spacecraft along a specific non-Keplerian orbit, such as a lunar pole-sitter orbit, which provides continuous coverage of the lunar South Pole. The solar-sail acceleration can also be used to displace the natural L_2 halo orbits by pitching the solar sail with respect to the Earth-Moon plane. A previously found constellation consisting of two solar-sail displaced L_2 vertical Lyapunov orbits can provide continuous coverage of both the lunar South Pole, and the Aitken basin at the far side of the Moon. Both spacecraft are placed in an identical orbit, but phased half a orbital period apart. The constellation is achievable with solar sails at a constant attitude profile, opposed to the lunar pole-sitter concept. In order to assess the feasibility of this constellation, the corresponding transfer trajectories starting from a parking orbit around Earth have to be designed, which in turn determines the injectable spacecraft mass and achievable transfer time.

The transfers have been found using reverse time propagations of the dynamics in the Earth-Moon circular restricted three-body problem, where the control is provided by a steering law. A locally optimal steering law allows for the quickest transfer trajectories, but requires rapid changes in attitude, which results in unfeasible singularities in the control history. Furthermore, the found trajectories require a long spiral Earth escape phase and are not connected to standard parking orbits. Nevertheless, the method provides continuous trajectories connected to the designated target orbits in the chaotic Earth-Moon system.

To further improve the design of these trajectories, the results found by applying the reverse time propagations are used as an initial guess for a 12^{th}-order Gauss-Lobatto collocation method. In this method, path and point constraints are incorporated, thereby increasing the feasibility of the results. The minimum altitudes with respect to the Earth and the Moon are constrained to 10 000 km and four lunar radii, respectively. The minimum altitude constraints eliminate low-altitude flybys, which can generate solar-sail drag or gravitational perturbations. In addition, a maximum sail rotation rate of 20 deg/day is enforced, to remove the control singularities introduced by the locally optimal steering law. The transfer time of the trajectories is reduced by allowing the spacecraft to depart from Soyuz's highly elliptical parking orbits, which are defined by a perigee altitude of 250 km, an inclination of 6 deg and an argument of perigee of 178 deg. The spacecraft depart from the highly elliptical orbit by deploying the solar sail eliminating the need for a kickstage.

The constraints are consecutively enforced, such that the effect on the performance of the transfer trajectory can be monitored. First, a map is generated by carrying out the reverse time propagations of the locally optimal steering law using 2000 trajectories. The shortest trajectory achieves a transfer within 50.7 days, while trajectories longer than one year are also found, containing the previously mention long duration spiral Earth escape phase departing from medium Earth orbits. Secondly, the feasibility of the found trajectories is improved by enforcing the altitude and departure point constraints. The fastest trajectory found using the collocation method completes the transfer within 39.6 days. If the rotation rate constraint is enforced as well, the transfer time increases to 41.8 days. Finally, sets of feasible trajectories for both spacecraft with identical launch conditions are sought, such that the constellation can be initiated using a single rocket launch. The Soyuz launch can deliver two 1160-kg

spacecraft in the fastest set of transfer trajectories, where the first spacecraft reaches its target orbit after 53.1 days, while the second spacecraft takes 67.9 days to complete its transfer.

This thesis shows that the 12^{th}-order Gauss-Lobatto collocation method is a powerful tool to find solar-sail transfer trajectories, while applying multiple path and point constraints on the trajectory. The research furthermore demonstrates that solar-sail transfer trajectories are feasible in the Earth-Moon system without requiring long transfer times, low-altitude flybys or singularities in the control.

Contents

List of Figures

Nomenclature

Latin symbols

A_i	=	matrix of polynomial coefficients
A_s	=	sail area
$\mathbf{a}$	=	acceleration vector
a	=	semi-major axis
$a_{0,EM}$	=	scaled characteristic sail acceleration
a_{EM}	=	characteristic sail acceleration
a_i	=	collocation method constant
B	=	constant matrix
$\mathbf{b}$	=	last column of B^{-1}
b_i	=	collocation method constant
C	=	dimensionless constant error estimation
$\mathbf{c}$	=	point constraints
$D\mathbf{F}$	=	Jacobi matrix
$D\mathbf{X}$	=	search direction
e	=	eccentricity
e_i	=	error over segment ”i”
$\mathbf{F}$	=	constraint vector
$\mathbf{F_i}$	=	constraint vector over segment ”i”
$\mathbf{f}$	=	EoM in ODE form
$\mathbf{g}$	=	path constraints
h	=	altitude
I	=	integral function
i	=	inclination
m_i	=	mass of body ”i”
$\hat{\mathbf{n}}$	=	solar sail normal direction
n	=	number of node points
P	=	period
P_{syn}	=	synodic period of the Sun
R_e	=	Earth radius
R_i	=	rotation matrix around axis ”i”
R_m	=	lunar radius
$\mathbf{r_i}$	=	radius vector of body ”i”
$\mathbf{r_{ij}}$	=	radius vector of body ”i” from body ”j”
$\hat{\mathbf{r}}_{\mathbf{43}}$	=	axis of Sun-sail frame
$\mathbf{t}$	=	time vector
$t_{arrival}$	=	arrival time
U	=	effective potential
U_{length}	=	length unit Earth-Moon system
U_{time}	=	time unit Earth-Moon system
$\mathbf{u}$	=	control vector
$\mathbf{v}$	=	velocity vector
v_i	=	collocation method constant
w_i	=	collocation method constant
$\mathbf{X}$	=	decision vector
$\mathbf{x}^{(8)}$	=	eight-order derivative of the state vector
$\mathbf{x_i}$	=	state vector for node ”i”
$\mathbf{x_i'}$	=	dimensionless time derivative state vector
$\mathbf{X_i}$	=	decision vector over segment ”i”
$\mathbf{y_i}$	=	dimensionless 7$^{\text{th}}$ derivative of polynomial

Greek symbols

α	=	cone angle
α_{ls}	=	line search multiplier
β_0	=	lightness number
Δt	=	time step
$\Delta t_{transfer,max}$	=	maximum allowable transfer time
$\Delta\phi_i$	=	sail rotation over segment ”i”
δ	=	clock angle
δ_{eq}	=	obliquity of Earth’s rotation axis
ϵ	=	small number (10^{-10})
$\boldsymbol{\zeta_i}$	=	defect constraints
ζ	=	parameter steering law
$\boldsymbol{\eta}$	=	slack variables
$\hat{\boldsymbol{\theta}}_{\mathbf{43}}$	=	axis of Sun-sail frame
θ	=	true anomaly
θ_8	=	approximation of $x^{(8)}$
θ_{S0}	=	angular progressing of Sun at t = 0
μ_{EM}	=	mass fraction of Earth-Moon system
μ_i	=	gravitational parameter of body ”i”
σ_s	=	sail loading
σ^*	=	critical sail loading
τ	=	normalized time over a single segment
$\hat{\boldsymbol{\varphi}}_{\mathbf{43}}$	=	axis of Sun-sail frame
$\varphi_{2,0}$	=	phase angle Moon
Ω	=	right ascension of ascending node
Ω_s	=	synodic angular rate of the Sun
$\boldsymbol{\omega}_{\mathbf{rot}}$	=	rotation vector of synodic reference frame
ω	=	argument of perigee

Abbreviations

CR3BP	=	circular restricted three body problem
ECI	=	Earth centered inertial refence frame
ECL	=	ecliptic reference frame
EoM	=	equations of motion
GTO	=	geostationary transfer orbit
HEO	=	highly elliptical orbit
IKAROS	=	Interplanetary Kite-craft Accelerated by Radiation Of the Sun
IRF	=	inertial reference frame
JAXA	=	Japan Aerospace Exploration Agency
NLP	=	nonlinear programming
ODE	=	ordinary differential equations
SC	=	spacecraft
SRP	=	solar radiation pressure
SSO	=	solar-sail displaced L2 vertical Lyapunov orbit
SSF	=	Sun sail fixed frame
SYN	=	synodic reference frame of Earth-Moon system

1 Introduction

This chapter introduces the concept of solar sailing and the background to the thesis work. First, the solar-sail mission and concept heritage is presented in section 1.1. Secondly, the application of solar sailing for lunar exploration is presented in section 1.2, followed by section 1.3 that covers the field of solar-sail trajectory design. The research questions are established in section 1.4. Finally, the structure of the thesis is presented in section 1.5.

1.1. Solar-sail heritage

Solar sails can provide a continuous thrust over the entire mission duration without consuming a propellant [1]. This continuous thrust enables spacecraft to travel along non-Keplerian orbits, optimized for a certain mission objective. This allows for the development of new mission concepts, as propellant consumption is no longer a limiting factor. The first mission using solar radiation pressure as the main propulsion system was JAXA's IKAROS mission [2]. In 2010, using a 16×16 m^2 solar sail, the IKAROS mission demonstrated that solar sails can be utilized during interplanetary transfers. IKAROS demonstrated several additional technologies, including the deployment mechanisms for the sail, the application of thin-film solar cells for power generation and cells with variable surface reflection properties for attitude control. The NanoSail-D2 mission was launched in 2011 and proved the concept of deorbiting spacecraft using a small solar sail [3]. The solar sail generated a thrust from solar radiation pressure, reducing the altitude of the spacecraft, while the large sail area also generated a significant drag force. A final additional solar-sail technical demonstration mission was LightSail-1 [4].

Some conceptual applications of solar-sail technology have recently received attention. The Lagrangian points in the Sun-Earth system can be displaced by applying a continuous thrust by means of a solar sail. For example, in the GeoStorm concept, the spacecraft is located at a sunward displaced L_1 point, which allows for increased warning times for solar activity [5]. Earlier detection of solar storms provides the opportunity for the implementation of more adequate countermeasures, limiting the risk to exposed spacecraft and Earth-based infrastructure. As another example, the solar-sail acceleration can also be used to counter Earth's gravity and place a spacecraft in a pole-sitter position. A solar sail placed in a pole-sitter position allows for continuous coverage of Earth's polar regions [6, 7], but are located at an altitude in the order of 3×10^6 km. A family of solar sail orbits in Ref. [8], provides continuous coverage of Earth's poles at lower altitudes, allowing for higher resolution imaging.

1.2. Lunar exploration and coverage

In addition to exploiting the solar-sail acceleration in the Sun-Earth system, the solar sail can also be used within the Earth-Moon system, to generate non-Keplerian orbits. One such example is the family found in Ref. [8] which provides coverage of the lunar South Pole as well as the far side of the Moon. The far side of the Moon is an interesting site for a future radio telescope, as it is shielded from Earth-based radio noise [9]. Furthermore, the Aitken Basin reveals deeper layers of the lunar crust, providing insight on the composition and origin of the Moon. Finally, the lunar South Pole is believed to contain water ice in its permanently shadowed crates and would thus be an interesting location for a future

human outpost [9]. For these proposed concepts, a satellite link is required that provides continuous communications with Earth.

Natural halo orbits at the Earth-Moon L_2 point have been considered to provide such a link between the far side of the Moon and the Earth. However, such orbits do not guarantee continuous coverage of the lunar South Pole [10]. In order to provide such continuous coverage, combinations of two halo, vertical, and butterfly orbits have been considered at the Earth-Moon L_1 and the L_2 points, which can achieve continuous coverage of the lunar South Pole [11]. Other studies have proposed a single lunar pole-sitter mission, where a solar sail is used to provide the required control acceleration to continuously hover below the South Pole of the Moon [12]. These orbits provide continuous coverage for the lunar South Pole, but provide no continuous coverage of the Aitken Basin.

A constellation of two spacecraft in solar-sail displaced L_2 vertical Lyapunov orbits found in Ref. [8] can achieve this needed continuous coverage of both the lunar South Pole and the Aitken Basin. The constellation requires a solar-sail characteristic acceleration of $0.3\,\mathrm{mm/s^2}$ and maintains a constant attitude with respect to the Sun, simplifying the attitude control of the solar sail. Although a detailed design of the orbits of the constellation has been conducted, the design of transfer trajectories to the constellation is still to be explored and will determine the feasibility of such a mission.

1.3. Solar-sail trajectory design

Previous solar-sail transfer trajectories have been designed using predefined steering laws [13]. The trajectories are then generated by reverse time propagations of the dynamics, where the defined steering law is used to provide the control. This results in spiral trajectories escaping Earth and reaching the targeted orbit. Various steering laws have been proposed such as the locally optimal steering law, the velocity tangent steering law or the on-off switching law [1]. These steering laws require fast rotations of the sail and result in unfeasible singularities in the control. Furthermore, the trajectories are not connected to standard parking orbits, which are often specified by a set perigee altitude, inclination and argument of perigee [14].

In order to address these discrepancies, constraints have to be imposed on the trajectory. Such solar-sail transfers have been successfully designed using multiple-shooting [7, 15] and collocation techniques [12]. Multiple-shooting techniques are fast to implement and can be designed using a small number of optimization variables. On the downside, they require significant computational power as every segment is integrated for each applied perturbation and can be very sensitive to small changes in the design variables [16]. Collocation methods allow for easy implementation of path and point constraints and do not require a separate integration of the dynamics [16]. Multiple Gauss-Lobatto collocation methods have been successfully implemented in Ref. [12] to find solar-sail orbits and trajectories. When employing the sparsity of the Jacobi matrix, problems containing 100 000 variables are permitted [16, 17]. Although the transfer trajectories found in Ref. [12] converged, no path constraints were enforced. The feasibility of solar-sail transfer trajectories can therefore be further improved by enforcing constraints on, for example, the minimum altitude with respect to Earth and the Moon, and on the maximum rotation rate of the solar sail.

1.4. Research questions

Based on the context in this chapter, the following research objective is defined:

The research objective of this thesis is to contribute to the development of solar-sail missions, by designing transfer trajectories to the constellation of solar-sail displaced L_2 vertical Lyapunov orbits in the Earth-Moon system, to support communication with the far side of the Moon as well as the lunar South Pole.

In order to assess the performance of the transfer trajectories, the transfer time and possible transfer mass for a given launcher will be calculated. Subsequently, constraints will be enforced in order to increase the feasibility of both the trajectory as well as the control history. Finally, for a realistic mission concept, both spacecraft of the constellation will have to be launched using a single rocket launch. In order to fulfill the research objective, the following main research question and research subquestions are formulated:

What are the achievable transfer times and spacecraft masses for a solar-sail trajectory from an Earth-based parking orbit to a constellation of solar-sail displaced L_2 vertical Lyapunov orbits in the Earth-Moon system?

a) What transfer time can be achieved by solving the trajectory problem through the application of locally optimal steering laws?

b) What transfer times can be achieved through the application of the 12th-order Gauss-Lobatto collocation method?

c) What is the effect on the found transfer trajectories if the maximum solar-sail rotation rate is constrained to 20 deg/day?

d) What is the performance of the found transfer trajectories in terms of spacecraft mass for a realistic mission scenario involving a single Soyuz launch?

By answering these research questions and fulfilling the research objective, feasible solar-sail transfer trajectories are designed, hereby contributing to the development of both future lunar and solar-sail missions.

1.5. Report outline

In order to answer the research questions and fulfill the research objective, this report's main body consists of a draft journal article containing the design and results of this thesis. The article briefly introduces the purpose of this work, followed by a section describing the solar-sail dynamics in the Earth-Moon system. The design and applications of the solar-sail displaced L_2 vertical Lyapunov orbits is discussed. This is followed by a section on the generation of an initial guess to the trajectory problem, a section on the collocation method and a section on mesh and error control. A separate section contains the detailed implementation of the algorithm leading to feasible solutions. Finally, the results section contains the found transfer trajectories. In addition to the conclusions in the paper, this report contains a separate conclusion and recommendation section where the research questions are answered and a reflection on the work is presented. To improve the credibility of this work, a verification and validation chapter is present in the appendix.

2

Journal article

Solar-sail transfers to Earth-Moon L_2-displaced vertical Lyapunov orbits

Thomas D. van den Oever[1]
Delft University of Technology, 2629 HS Delft, the Netherlands

This paper presents the design of solar-sail transfer trajectories to a constellation of two spacecraft in displaced vertical Lyapunov orbits at the L_2 point of the Earth-Moon system. The constellation provides continuous coverage of the Aitken basin and the lunar South Pole. Initial guesses for the transfers are generated using reverse time propagations of the dynamics, where the control is provided by a locally optimal steering law. These initial guesses are subsequently used to initialize a 12^{th}-order Gauss-Lobatto collocation method. The minimum altitude with respect to the Earth and the Moon are constrained, as well as the maximum rotation rate of the solar sail. Sets of feasible trajectories for both spacecraft with identical launch conditions are sought, such that the constellation can be initiated using a single Soyuz launch. Such a Soyuz launch can deliver two 1160-kg spacecraft into the found transfer trajectories. The first spacecraft subsequently requires a transfer time of 53.06 days to enter its constellation orbit, while the transfer of the second spacecraft takes 67.89 days. This research demonstrates that solar-sail transfer trajectories are a feasible option for future missions in the Earth-Moon system.

---

[1] MSc. Student, Faculty of Aerospace Engineering, Kluyverweg 1

Nomenclature

A_i	= matrix of polynomial coefficients	P	= period
A_s	= sail area	P_{syn}	= synodic period of the Sun
$\mathbf{a}$	= acceleration vector	R_e	= Earth radius
a	= semi-major axis	R_i	= rotation matrix around axis "i"
$a_{0,EM}$	= scaled characteristic sail acceleration	R_m	= lunar radius
a_{EM}	= scaled characteristic sail acceleration	$\mathbf{r_i}$	= radius vector of body "i"
a_i	= collocation method constant	$\mathbf{r_{ij}}$	= radius vector of body "i" from body "j"
B	= constant matrix	$\hat{\mathbf{r}}_{\mathbf{43}}$	= axis of Sun-sail frame
$\mathbf{b}$	= last column of B^{-1}	$\mathbf{t}$	= time vector
b_i	= collocation method constant	$t_{arrival}$	= arrival time
C	= dimensionless constant error estimation	U	= effective potential
$\mathbf{c}$	= point constraints	U_{length}	= length unit Earth-Moon system
$D\mathbf{F}$	= Jacobi matrix	U_{time}	= time unit Earth-Moon system
$D\mathbf{X}$	= search direction	$\mathbf{u}$	= control vector
e	= eccentricity	$\mathbf{v}$	= velocity vector
e_i	= error over segment "i"	v_i	= collocation method constant
$\mathbf{F}$	= constraint vector	w_i	= collocation method constant
$\mathbf{F_i}$	= constraint vector over segment "i"	$\mathbf{X}$	= decision vector
$\mathbf{f}$	= EoM in ODE form	$\mathbf{x^{(8)}}$	= eight-order derivative of the state vector
$\mathbf{g}$	= path constraints	$\mathbf{x_i}$	= state vector for node "i"
h	= altitude	$\mathbf{x_i'}$	= dimensionless time derivative state vector
I	= integral function	$\mathbf{X_i}$	= decision vector over segment "i"
i	= inclination	$\mathbf{y_i}$	= dimensionless 7^{th} derivative of polynomial
m_i	= mass of body "i"	α	= cone angle
$\hat{\mathbf{n}}$	= solar sail normal direction	α_{ls}	= line search multiplier
n	= number of node points	β_0	= lightness number

Δt	= time step	θ_{S0}	= angular progressing of Sun at t = 0
$\Delta t_{transfer,max}$	= maximum allowable transfer time	μ_{EM}	= mass fraction of Earth-Moon system
$\Delta\phi_i$	= sail rotation over segment "i"	μ_i	= gravitational parameter of body "i"
δ	= clock angle	σ_s	= sail loading
δ_{eq}	= obliquity of Earth's rotation axis	σ^*	= critical sail loading
ϵ	= small number (10^{-10})	τ	= normalized time over a single segment
$\boldsymbol{\zeta_i}$	= defect constraints	$\hat{\boldsymbol{\varphi}}_{\mathbf{43}}$	= axis of Sun-sail frame
ζ	= parameter steering law	$\varphi_{2,0}$	= phase angle Moon
$\boldsymbol{\eta}$	= slack variables	Ω	= right ascension of ascending node
$\hat{\boldsymbol{\theta}}_{\mathbf{43}}$	= axis of Sun-sail frame	Ω_s	= synodic angular rate of the Sun
θ	= true anomaly	$\boldsymbol{\omega}_{\mathbf{rot}}$	= rotation vector of synodic reference frame
θ_8	= approximation of $x^{(8)}$	ω	= argument of perigee

I. Introduction

Recent developments in solar-sail technology grant opportunities for the advancement of new mission concepts. The advantage of employing a solar sail is that a continuous acceleration can be provided without the demand for a mass-consuming propulsion system [1]. This allows for new types of non-Keplerian orbits and trajectories that are optimized for specific mission objectives, such as the coverage of specific areas on the Earth [2, 3], the Moon [4, 5] and other celestial bodies [6], shorter transfer times [7] or longer orbital lifetimes [4]. For example, in the GeoStorm concept, the spacecraft is located at a sunward displaced L_1 point, which allows for increased warning times for solar activity [8]; a solar-sail pole-sitter allows for continuous coverage of Earth's poles with a single spacecraft without the need for a propellant [2, 6]; and, finally, the family of solar-sail displaced L_2 vertical Lyapunov orbits (SSOs) found in Ref. [4], can be used to provide continuous coverage of interesting features on the Moon (including the Aitken Basin and the lunar South Pole). The Aitken Basin is scientifically interesting as it reveals deeper layers of lunar crust [9]. Also, the far-side of the Moon is a perfect site for a radio-telescope as it is continuously shielded from Earth-based radio noise and can thus study signals that can otherwise not be detected [9]. Finally,

the lunar South Pole could host a future permanent human outpost, as it is continuously lit by sunlight, which can provide power, and water ice is believed to exist in its permanently shadowed lunar craters [9]. For these proposed lunar mission concepts, a satellite uplink is required to provide communications with Earth. When using a constellation of two spacecraft in the SSOs found in Ref. [4], continuous coverage can be provided of the Aitken basin and the lunar South Pole, while maintaining a permanent view of the Earth.

The purpose of this paper is to find feasible transfer trajectories from Earth to the proposed constellation in Ref. [4]. By designing the transfer trajectory, the feasibility and performance of the proposed constellation can be assessed, such as the available mass budget and the achievable transfer time. Previous solar-sail transfer trajectories have been designed using locally optimal steering laws [10–12], including transfers in the Earth-Moon system [13] or using the velocity tangent steering law refined with collocation techniques [5]. These methods result in trajectories connecting a parking orbit such as geostationary transfer orbit (GTO) with a target orbit in the Earth-Moon system, but contain discontinuities in the sail attitude and require long transfer times.

To further improve the design of solar-sail transfer trajectories, this paper develops a collocation method with additional path and point constraints and applies it to the L_2 constellation. Initial guesses are generated by reverse time propagations of the dynamics in the circular restricted three-body problem, where the control is provided by the locally optimal steering law. In order to enforce constraints on the found trajectories, the 12^{th}-order Gauss-Lobatto collocation method is applied to transcript the trajectory to a nonlinear programming (NLP) problem [14, 15]. Collocation methods can incorporate path and point constraints and contrary to multiple shooting methods, do not require an explicit integration of the dynamics. Collocation methods also have a wider radius of convergence than multiple shooting methods, as the sensitivity of the trajectory is distributed over more segments [16]. In order to improve the radius of convergence and accuracy even further, an error estimation scheme based on Ref. [17] is applied in order to refine the mesh and equidistribute the error. Consecutively, the NLP-problem is solved using the multivariate Gauss-Newton algorithm [18] in conjunction with a line search method [16]. In order to find feasible trajectories, the maximum rotation rate of the sail is constrained to 20 deg/day. Furthermore, the minimum altitude with

respect to the Earth is set to 10 000 km and to four lunar radii with respect to the Moon. The departure point of the transfer trajectory is constraint to belong to an Highly Elliptical Orbit (HEO) of a Soyuz launcher [19], while the arrival point is enforced to match both the states and control of the SSO. Note that during the first day of the trajectory no solar-sail acceleration is generated, to allow for solar sail deployment. Once a feasible trajectory is found for the first spacecraft, a similar trajectory with identical launching conditions is sought for the second spacecraft. By designing both trajectories for the constellation with identical launching conditions, a feasible mission scenario using a single Soyuz launch results. Finally, for this feasible mission scenario, a preliminary mass budget is constructed based on reference satellites.

II. Dynamics

The dynamics of the transfer trajectory are modelled in the framework of the circular restricted three-body problem (CR3BP), taking into account the gravity of the Earth and Moon, as well as the solar radiation pressure (SRP) originating from the Sun. This section will first discuss the dynamics of the CR3BP, followed by a model for the ideal solar-sail acceleration. Finally, the motion of the Sun with respect to Earth-Moon system is described.

A. Circular restricted three-body problem

At large distances from the Earth, such as distances beyond geostationary Earth orbit (GEO) altitude, the gravitational pull of the Moon can no longer be neglected and requires to be included in the spacecraft dynamics. The dynamics concerning three bodies are modelled through the CR3BP, similar to the proposed constellation in Ref. [4] and considers the Earth (body 1), the Moon (body 2) and the spacecraft (body 3). The CR3BP utilizes a synodic reference frame (SYN) shown in Fig. 1. The origin of the SYN frame is located at the Earth-Moon barycenter. The $\hat{\mathbf{x}}_{SYN}$-axis is aligned with the Earth-Moon line, while the $\hat{\mathbf{z}}_{SYN}$ is perpendicular to the Earth-Moon orbital plane and coincides with the rotational direction of the reference frame, $\omega_{\mathbf{rot}}$. Subsequently, the $\hat{\mathbf{y}}_{SYN}$ completes the right-handed reference frame.

In the CR3BP, the distances, time and mass are made dimensionless. Distances are made dimensionless by taking the Earth-Moon distance as the length unit (U_{length}). This results in the

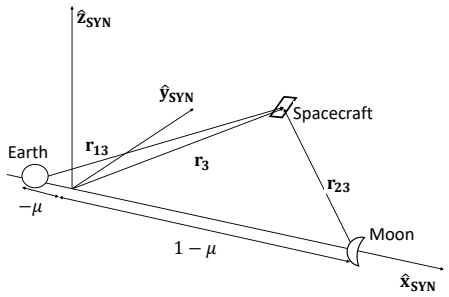

Fig. 1 Synodic reference frame employed by the CR3BP.

Earth being located at $x_{SYN} = -\mu_{EM}$ and the Moon at $x_{SYN} = 1 - \mu_{EM}$, where the mass fraction μ_{EM} is calculated using:

$$\mu_{EM} = \frac{m_2}{m_1 + m_2}. \tag{1}$$

Similarly, the time unit (U_{time}) is scaled such that the rotational velocity of the Earth-Moon system becomes 1/rad. The constants given in Tab. 1 are used to model the Earth-Moon system.

Table 1 Parameters for the CR3BP involving the Earth and the Moon, provided by Ref. [20]. The period is calculated using the 2-body period of the Moon around the Earth [4].

Parameter	Value	Unit	Description
m_1	$5.9723 \cdot 10^{24}$	kg	mass Earth
m_2	$0.07346 \cdot 10^{24}$	kg	mass Moon
μ_{EM}	0.01215	-	mass fraction according to Eq. 1
r_{12}	$0.3844 \cdot 10^{6}$	km	Earth-Moon distance
P_M	27.4520	days	2-body period of the Moon's orbit around the Earth
U_{length}	$0.3844 \cdot 10^{6}$	km	dimensionless distance unit
U_{time}	$0.3775 \cdot 10^{6}$	s	dimensionless time unit

The framework of the CR3BP exists under a set of assumptions. First of all, the orbits of the Earth and Moon are assumed to be both coplanar and circular around their common barycenter. Secondly, the gravitational potential of the Earth and Moon can be approximated as point masses. Finally, the mass m_3 of the spacecraft is much smaller than the masses of the Earth and the Moon such that ($m_3/m_1 \approx m_3/m_2 \approx 0$). Using these assumptions, the equations of motion (EoM) in the

CR3BP are given by [2]:

$$\ddot{\mathbf{r}}_{\mathbf{3}} + 2\boldsymbol{\omega}_{\boldsymbol{rot}} \times \dot{\mathbf{r}}_{\mathbf{3}} = -\nabla U(\mathbf{r}_{\mathbf{3}}) + \mathbf{a}(t), \tag{2}$$

where $\mathbf{r_3}$ is the position vector of the solar sail with respect to the SYN frame, $\boldsymbol{\omega_{rot}}$ is the rotation vector of the SYN frame equal to $\begin{bmatrix} 0 & 0 & 1 \end{bmatrix}^T$ and $\mathbf{a}$ is the sum of additional acceleration terms containing, in this paper, the solar-sail induced acceleration. U is the sum of the gravitational and centripetal potentials which is given by:

$$U(\mathbf{r_3}) = -\frac{1-\mu_{EM}}{r_{13}} - \frac{\mu_{EM}}{r_{23}} - \frac{x_3^2 + y_3^2}{2}, \tag{3}$$

$$\mathbf{r_{13}} = \mathbf{r_3} + \begin{bmatrix} \mu_{EM} & 0 & 0 \end{bmatrix}^T, \tag{4}$$

and

$$\mathbf{r_{23}} = \mathbf{r_3} - \begin{bmatrix} 1-\mu_{EM} & 0 & 0 \end{bmatrix}^T, \tag{5}$$

where $\mathbf{r_{13}}$ and $\mathbf{r_{23}}$ are the radius vectors of the spacecraft with respect to the Earth and the Moon. Using U, Eq. 2 can be rewritten as a set of ordinary differential equations $\frac{d\mathbf{x}}{dt} = \mathbf{f}(t, \mathbf{x}, \mathbf{u})$ with state vector $\mathbf{x} = \begin{bmatrix} \mathbf{r_3}^T & \dot{\mathbf{r}}_{\mathbf{3}}^T \end{bmatrix}^T$, which can be explicitly integrated if the solar-sail acceleration in the term $\mathbf{a}(t)$ is known.

B. Solar-sail acceleration

Momentum carried by solar photons can be exchanged with an object by reflecting, absorbing and re-radiating these photons. This principle can be exploited as a propulsion method by utilizing a thin, large, reflective surface called a solar sail. In this work, an ideal solar sail is assumed, where every photon is reflected specularly. In that case, the acceleration produced by the solar radiation pressure (SRP) acts along the sail normal direction $\hat{\mathbf{n}}$. The resulting acceleration is thus a function of the orientation of the sail. In order to describe this orientation with respect to the Sun, a new Sun-sail fixed reference frame, SSF$\left(\hat{\mathbf{r}}_{\mathbf{43}}, \hat{\theta}_{\mathbf{43}}, \hat{\varphi}_{\mathbf{43}}\right)$, is defined [2], see Fig. 2. The $\hat{\mathbf{r}}_{\mathbf{43}}$-axis is defined along the incoming SRP direction:

$$[\hat{\mathbf{r}}_{\mathbf{43}}]_{SYN} = \frac{[\mathbf{r_{43}}]_{SYN}}{|[\mathbf{r_{43}}]_{SYN}|}. \tag{6}$$

The other two axes, $\hat{\theta}_{\mathbf{43}}$ and $\hat{\varphi}_{\mathbf{43}}$, are defined as:

$$[\hat{\theta}_{\mathbf{43}}]_{SYN} = \frac{[\hat{\mathbf{z}}]_{SYN} \times [\hat{\mathbf{r}}_{\mathbf{43}}]_{SYN}}{|[\hat{\mathbf{z}}]_{SYN} \times [\hat{\mathbf{r}}_{\mathbf{43}}]_{SYN}|}, \tag{7}$$

and

$$[\hat{\varphi}_{\mathbf{43}}]_{SYN} = [\hat{\mathbf{r}}_{\mathbf{43}}]_{SYN} \times [\hat{\theta}_{\mathbf{43}}]_{SYN}. \tag{8}$$

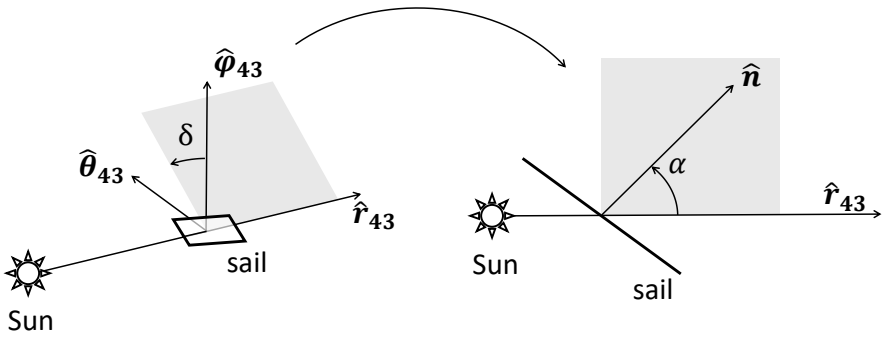

Fig. 2 Sun sail fixed (SSF) reference frame.

Using the three reference directions, expressed in Cartesian coordinates, the rotation matrix from frame SYN to SSF is given by:

$$[\hat{\mathbf{n}}]_{SYN} = \left[[\hat{\mathbf{r}}_{\mathbf{43}}]_{SYN} \;\; [\hat{\theta}_{\mathbf{43}}]_{SYN} \;\; [\hat{\varphi}_{\mathbf{43}}]_{SYN} \right] [\hat{\mathbf{n}}]_{SSF} \tag{9}$$

The orientation of the sail normal can be defined with respect to the SSF frame by two rotations. First, a rotation around the $\hat{\mathbf{r}}_{\mathbf{43}}$-axis over the clock angle δ defines a new surface. On this surface, the cone angle α pitches the solar sail with respect to the Sun-sail line. The Cartesian elements of the resulting normal vector are then given by:

$$[\hat{\mathbf{n}}]_{SSF} = R_1(-\delta)R_2(-\alpha) \begin{bmatrix} 1 & 0 & 0 \end{bmatrix}^T = \begin{bmatrix} \cos(\alpha) & \sin(\alpha)\sin(\delta) & \sin(\alpha)\cos(\delta) \end{bmatrix}^T, \tag{10}$$

which can be used to calculate the solar-sail acceleration:

$$\mathbf{a_{SRP}} = a_{0,EM}(\hat{\mathbf{r}}_{\mathbf{43}} \cdot \hat{\mathbf{n}})^2 \hat{\mathbf{n}}. \tag{11}$$

The characteristic solar-sail acceleration ($a_{0,EM}$) is the maximum achievable solar-sail acceleration for a given spacecraft mass and solar sail size. As the SRP induced acceleration always cannot act in direction of the Sun, the domain of the cone angle is limited to 0 deg $\leq \alpha \leq$ 90 deg. The constellation in Ref. [4] requires a value for $a_{0,EM}$ of 0.1 in dimensionless units, which will be used throughout this report. It is assumed that the spacecraft mass, solar sail size and solar radiation pressure in the Earth-Moon system are constants, resulting in a constant $a_{0,EM}$. If the position of the Sun with respect to the SYN frame is known, i.e. $\hat{\mathbf{r}}_{\mathbf{43}}$, the solar-sail acceleration can be calculated.

C. Motion of the Sun

The Earth-Moon system orbits around the Sun, which causes the direction of the SRP in the synodic reference frame to change over time. In this work, it is assumed that the orbit of the Earth-Moon barycenter around the Sun is circular and that it is coplanar with the Earth-Moon orbital plane. This results in a clockwise, circular motion of the Sun in the $(\hat{\mathbf{x}}_{SYN}, \hat{\mathbf{y}}_{SYN})$-plane around the Earth-Moon barycenter [4], see Fig. 3.

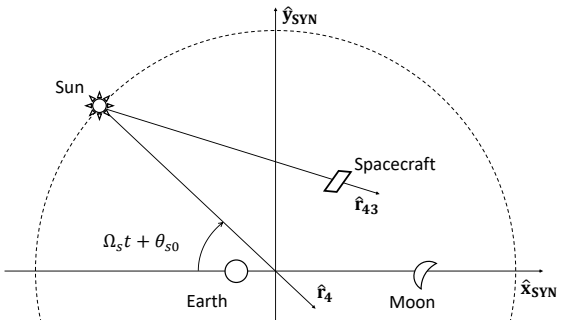

Fig. 3 Earth-Moon synodic reference frame with position of the Sun.

The position of the Sun is determined by the angular progression of the Moon around Earth and the angular progression of the Earth around the Sun. Therefore, the synodic angular velocity of the Sun Ω_S is used to determine the position of the Sun as a function of time, which is calculated using:

$$P_{syn} = \frac{1}{\frac{1}{P_M} - \frac{1}{P_E}} \tag{12}$$

and

$$\Omega_S = \frac{2\pi}{P_{syn}}. \tag{13}$$

The periods of Earth's orbit around the Sun, P_E, and the Moon's orbit around the Earth, P_M, can be seen in Table 2. The direction of the SRP in the synodic reference frame can then be described

Table 2 Periods and angular velocities of the orbits of the Earth, Moon and Sun [20].

Parameter	Values	Unit	Description
P_E	365.256	days	Orbital period Earth
P_M	27.3217	days	Orbital period Moon
P_{syn}	29.5306	days	Sun's synodic period
Ω_S	$2.4626 \cdot 10^{-6}$	rad/s	Angular rate Sun in SYN frame
Ω_S	0.9252	rad/−	Dimensionless angular rate Sun in SYN frame

with [4]:

$$[\hat{\mathbf{r}}_\mathbf{4}]_{SYN} = -\begin{bmatrix}\cos(\Omega_s t + \theta_{s,0}) & -\sin(\Omega_s t + \theta_{s,0}) & 0\end{bmatrix}^T, \tag{14}$$

where $\theta_{s,0}$ is the angular progression of the Sun at $t = 0$ since the last full Moon. During this work, it is assumed that the distances in the Earth-Moon system are small with respect to the Sun-Earth distance, resulting in: $\hat{\mathbf{r}}_\mathbf{34} \approx \hat{\mathbf{r}}_\mathbf{4}$. With $\hat{\mathbf{r}}_\mathbf{4}$ known, the solar-sail acceleration in Eq. 11 can be evaluated for a given normal vector. If a steering law for the normal direction of the sail is assumed, the differential equations in Eq. 2 can be integrated to find the corresponding solar-sail trajectory.

III. Problem description

As highlighted in the introduction, this paper searches for transfers between an Earth-based parking orbit and solar-sail displaced L_2 vertical Lyapunov orbits (SSOs). In this section, the departure and arrival conditions of the trajectories are discussed. First, the design of the SSOs is presented. Secondly, the geometry of the parking orbit is given, followed by the general layout of the transfer trajectory. Finally, the required transformations are given to determine the orbital elements of the departure point in the Earth Centered Inertial (ECI) frame.

A. Solar-sail displaced L_2 vertical Lyapunov orbits

Solar sails can be used to create families of non-Keplerian orbits [4]. One such family of orbits is found starting from a classical Earth-Moon L_2 vertical Lyapunov orbit with a period (P_{SSO}) equal to $2P_{SYN} = 59.34$ days. Using a stepwise increase in the characteristic acceleration of the sail $a_{0,EM}$, in combination with a differential correction technique, the trajectory is slightly displaced from the classical orbit. In particular, the solar sail is pitched at an angle of $\alpha = -35.26\,\text{deg}$ with respect to the Earth-Moon orbital plane in order to increase the out-of-plane acceleration, such that the found orbits are displaced towards the Southern hemisphere of the Moon to provide better lunar South Pole coverage. The resulting family of orbits is shown in Fig. 4 as a function of the dimensionless characteristic solar-sail acceleration $a_{0,EM}$ in the SYN frame.

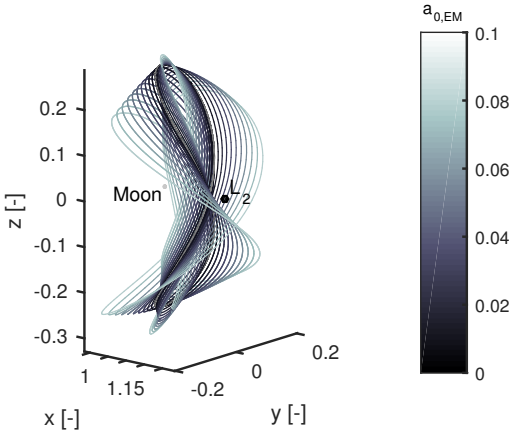

Fig. 4 Family of solar-sail L_2-displaced vertical Lyapunov orbits in the SYN frame, as function of $a_{0,EM}$. Taken from Ref. [4]

Using a constellation of two solar-sail spacecraft with $a_{0,EM} = 0.1$, it is possible to provide continuous coverage of the Aitken basin and the lunar South Pole, as well as maintaining a direct link with the Earth [4]. The two spacecraft, SC1 and SC2, are placed in identical orbits with a phase difference of half an orbital period which equals 29.67 days. In order to advance the development of this proposed constellation this paper will contain the design of feasible transfer trajectories to these orbits.

B. Earth-centered Highly Elliptical Orbits

The initial parking orbit for the spacecraft is assumed to be a Soyuz highly elliptical orbit (HEO). The geometry of the HEO is described using Keplerian elements expressed in the Earth Centered Inertial (ECI) reference frame [21, 22]. The HEOs have a perigee altitude of 250 km, an argument of perigee of 178 deg and an inclination of 6 deg. The other Keplerian elements, such as the apogee altitude, true anomaly and right ascension of ascending node can be chosen freely. The transfer mass of the Soyuz rocket to this family of HEOs as a function of the apogee altitude is given in Fig. 5 [19].

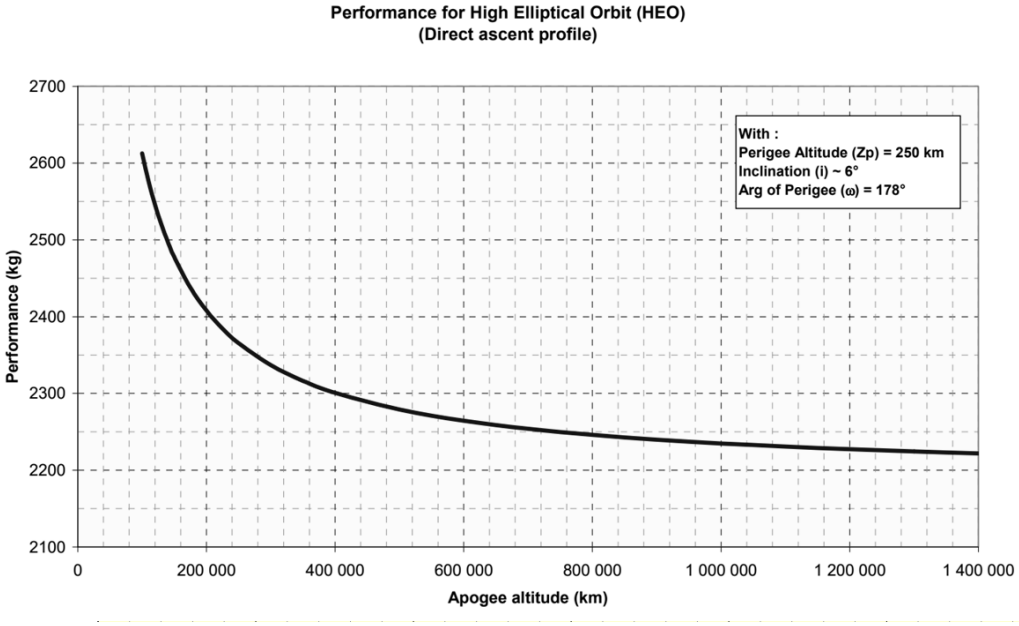

Fig. 5 Transfer mass to HEO as a function of apogee altitude for a Soyuz launch from Guiana Space Centre [19].

C. Trajectory design

The trajectories contains various segments which are shown in Fig. 6.

The initial HEO is described using Keplerian elements, which adhere to 2-body dynamics. It is assumed that the spacecraft departs from the HEO at geostationary Earth orbit (GEO) altitude, where a switch is made to 3-body dynamics, including the gravitational pull of the Moon. The first day of the trajectory is modelled as a ballistic segment to allow the sail to deploy. After the

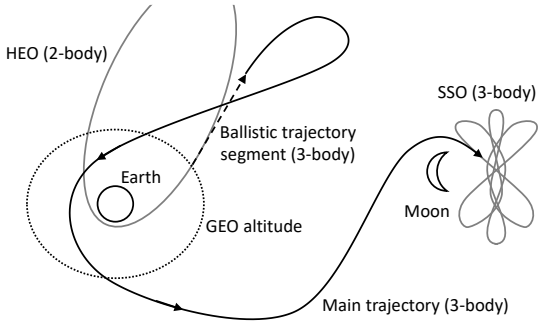

Fig. 6 Design of the transfer trajectory, including various trajectory segments.

first day, the solar sail is deployed and the main part of the trajectory will be propagated, until the trajectory arrives at the SSO.

D. Reference frame transformations

In order to connect the initial condition of the transfer trajectory to the HEOs in section III B, its Cartesian elements in the SYN frame are transformed to Keplerian with respect to the ECI frame. The first step in this transformation is to transform the spacecrafts position vector with respect to Earth $\mathbf{r_{13}}$ from the SYN frame to the ecliptic (ECL) reference frame. The ECL frame is an Earth-centered pseudo-inertial right-handed reference frame, where the x-axis is coincides with the vernal equinox and the z-axis is aligned with the angular momentum vector of Earth's orbit around the Sun [21]. The transformation from the SYN frame to the ECL frame is given as:

$$[\mathbf{r_3}]_{ECL} = R_3(\Omega_2)R_1(i_2)R_3(\omega_2 + \theta_2(t))[\mathbf{r_{13}}]_{SYN} \cdot U_{length}. \tag{15}$$

Similarly for the velocity vector $\dot{\mathbf{r}}_\mathbf{3}$:

$$[\dot{\mathbf{r}}_\mathbf{3}]_{ECL} = R_3(\Omega_2)R_1(i_2)R_3(\omega_2 + \theta_2(t))\left([\dot{\mathbf{r}}_\mathbf{3}]_{SYN} + \boldsymbol{\omega}_\mathbf{rot} \times [\mathbf{r_3}]_{SYN}\right) \cdot \frac{U_{length}}{U_{time}}, \tag{16}$$

where $R_j(\Psi)$ is a clockwise rotation matrix of angle Ψ around the 'j$^{\text{th}}$'-axis of a right-handed reference frame. Ω_2, i_2, ω_2 and θ_2 stand for the right ascension of ascending node, inclination, argument of perigee and true anomaly of the Moon with respect to the ECL frame. Since the angular progression of the Moon's orbit is equal to the time unit in the CR3BP, $\theta_2(t) = \theta_{2,0} + t$, where $\theta_{2,0}$ is the true anomaly of the Moon at $t = 0$. The Moon has an inclination of 5.145 deg with respect to the ecliptic, however, during this work it is assumed that the Moon's orbit coincides with

the ecliptic plane, resulting in a lunar inclination of 0 deg. For this inclination, Ω_2, ω_2 and θ_2 are not defined and are thus replaced replaced by a fixed phase angle $\varphi_{2,0} = \Omega_2 + \omega_2 + \theta_{2,0}$, which is assumed to be constant over the course of a trajectory. As a result, the rotational matrices in Eq. 15 and 16 can be rewritten as:

$$R_3(\Omega_2)R_1(i_2)R_3(\omega_2 + \theta_2(t)) = R_3(\varphi_{2,0} + t). \tag{17}$$

The coordinates expressed in the ECL frame, are then transformed to the ECI frame using:

$$[\mathbf{r_3}]_{ECI} = R_1(\delta_{eq})[\mathbf{r_3}]_{ECL}, \tag{18}$$

and

$$[\dot{\mathbf{r}}_\mathbf{3}]_{ECI} = R_1(\delta_{eq})[\dot{\mathbf{r}}_\mathbf{3}]_{ECL}, \tag{19}$$

where δ_{eq} is the obliquity of Earth's rotation axis equal to 23.44 deg [20]. The Cartesian state 6×1 vector $\begin{bmatrix} [\mathbf{r_3}]^T_{ECI} & [\mathbf{v_3}]^T_{ECI} \end{bmatrix}^T$ can then be transformed to find the Keplerian elements of the corresponding parking orbit.

IV. Initial guess generation

In order to design feasible transfer trajectories to the SSOs introduced in subsection III A, initial guesses are first generated. Due to the chaotic nature of the CR3BP, it is challenging to find trajectories departing from Earth and arriving at the SSO by just varying the conditions of the departure point and assuming a particular steering law. Therefore, instead, the trajectory is designed by selecting a state vector along the SSO, from which the dynamics are propagated backwards in time while reducing the energy with respect to Earth. The integration is terminated if a set altitude is reached, resulting in an initial guess for the trajectory. Along this trajectory a locally optimal steering law (LOSL) is used to determine the optimal sail attitude.

The LOSL determines this optimal sail attitude, by maximizing the solar-sail acceleration along the velocity vector $\left[\mathbf{v_3}\right]_{SSF}$ for every point along the trajectory. A complete derivation of the LOSL can be found in Ref. [1]. Here, only the result is presented. To compute the optimal attitude, first

the velocity vector is transformed to the SSF frame, using Eq. 20:

$$\begin{bmatrix} v_{x,SSF} \\ v_{y,SSF} \\ v_{z,SSF} \end{bmatrix} = [\mathbf{v_3}]_{SSF} = \begin{bmatrix} \hat{\mathbf{r}}_{\mathbf{43}} & \hat{\theta}_{\mathbf{43}} & \hat{\varphi}_{\mathbf{43}} \end{bmatrix}^T_{SYN} ([\mathbf{v_3}]_{SYN} + \omega_{\mathbf{rot}} \times [\mathbf{r_3}]_{SYN}). \tag{20}$$

Secondly, the parameter ζ is calculated as a function of the velocity components:

$$\zeta = \frac{-3v_{x,SSF}v_{y,SSF} \pm v_{y,SSF}\sqrt{9v^2_{x,SSF} + 8(v^2_{y,SSF} + v^2_{z,SSF})}}{4(v^2_{y,SSF} + v^2_{z,SSF})}, \tag{21}$$

which results in two values for ζ due to the $\pm$ sign. Both values of ζ are used to evaluate the desired sail orientation using:

$$n_{x,SSF} = \frac{|v_{y,SSF}|}{\sqrt{v^2_{y,SSF} + \zeta^2(v^2_{y,SSF} + v^2_{z,SSF})}}, \tag{22}$$

$$n_{y,SSF} = \zeta n_{x,SSF} \tag{23}$$

and

$$n_{z,SSF} = \frac{v_{z,SSF}}{v_{y,SSF}} n_{y,SSF}. \tag{24}$$

From the two solutions found, the attitude is selected which maximizes the acceleration along the velocity vector:

$$\mathbf{a_s}^T[\mathbf{v}]_{SSF} = a_{0,EM} n^2_{x,SSF}(n_{x,SSF}v_{x,SSF} + n_{y,SSF}v_{y,SSF} + n_{z,SSF}v_{z,SSF}). \tag{25}$$

The LOSL allows for a larger SRP acceleration along the velocity direction than other steering laws, such as the velocity tangent steering law or the on-off switching law also described by Ref [1]. The LOSL can generate small accelerations along the velocity direction, even if the spacecraft is moving towards the Sun. The found trajectories adhere to the dynamics, but contain attitude singularities, perform flybys at unfeasible altitudes and do not depart from Soyuz HEOs.

V. Trajectory transcription

In order to increase the feasibility of the found transfer trajectories, additional path and point constraints need to be enforced along the trajectory. The trajectory optimization problem contains an infinite number of dimensions, since the states and controls are described by continuous functions. In this section, the 12^{th}-order Gauss-Lobatto collocation method is described, which approximates these continuous functions using 7^{th}-degree piecewise polynomials. The continuous trajectory problem then reduces to finding a finite number of polynomials. A set of defect constraints is enforced over these polynomials such that the dynamics are satisfied. Furthermore, path and point constraints are added, resulting in a collection of constraints as a function of the states and controls. The trajectory optimization problem is thus rewritten as a non-linear programming (NLP) problem, which is consequently solved using the Gauss-Newton algorithm in conjunction with a line search method.

A. 12^{th}-order Gauss-Lobatto collocation method

The 12^{th}-order Gauss-Lobatto collocation method is described in detail in Ref. [14] and is applied to a solar-sail trajectory problem in Ref. [5]. Higher-order methods, like the 12^{th}-order Gauss-Lobatto collocation method, provide accurate solutions with fewer variables than lower-order methods, such as trapezoid and Hermite-Simpson methods [23]. Furthermore, the required computation time for higher-order methods is significantly lower than the required computation time for lower-order methods.

The method starts by diving the trajectory into n nodes, connected by $n-1$ segments as illustrated using Fig. 7(a), where every segment is described by a 7^{th}-degree piecewise polynomial, as shown in Fig. 7(b). The polynomial in Fig. 7(b) can be determined by evaluating both the states and dynamics at the two node points, which would result in a 3^{rd}-degree polynomial. In order to increase the degree and thus accuracy of the interpolating polynomial, two internal points are added, namely $\mathbf{x_{i2}}$ and $\mathbf{x_{i3}}$, which results in a 7^{th}-degree polynomial. In addition, three collocation points $\mathbf{x_{i1}}$, $\mathbf{x_{ic}}$ and $\mathbf{x_{i4}}$ are added, that are used to evaluate the dynamics and increase the accuracy of the method to $O(\Delta t^{12})$ [14].

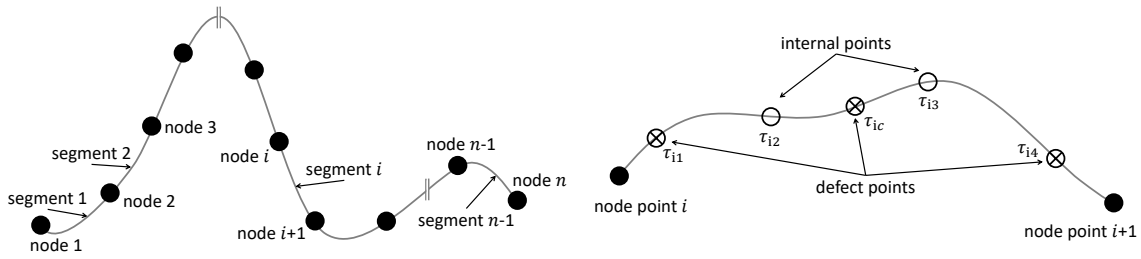

(a) (b)

Fig. 7 a) Trajectory divided into nodes and segments. b) Single segment described by a piecewise polynomial as applied in the Gauss-Lobatto method.

Table 3 Position of internal and collocation points along τ. [5, 14, 15]

Parameter	Type of point	Value
τ_i	node	0
τ_{i1}	defect	8.48880518607166e-2
τ_{i2}	internal	2.65575603264643e-1
τ_{ic}	defect	5.00000000000000e-1
τ_{i3}	internal	7.34424396735357e-1
τ_{i4}	defect	9.15111948139283e-1
τ_{i+1}	node	1

The position of the internal and defect points along the segment are given by the parameter τ:

$$\tau_{ik} = \frac{t_k - t_i}{\Delta t_i}, \tag{26}$$

where Δt_i is the timestep over the i^{th} segment, t_k is the time of the k^{th} internal or defect point along the segment and t_i is the time of the i^{th} node point. Values of τ for the internal and defect points are given in Table 3.

The six polynomials representing the six states over a segment are described by:

$$\mathbf{x_i}(\tau) = A_i \begin{bmatrix} 1 & \tau & \tau^2 & \tau^3 & \tau^4 & \tau^5 & \tau^6 & \tau^7 \end{bmatrix}^T. \tag{27}$$

where the 8×6 matrix A_i contains the eight coefficients of each 7^{th}-degree polynomial for the six states on segment i. Matrix A_i can be extracted by matching the polynomial with the states and

normalized dynamics at the node and internal points:

$$A_i B = \left[\mathbf{x_i} \;\; \mathbf{x_i'} \;\; \mathbf{x_{i2}} \;\; \mathbf{x_{i2}'} \;\; \mathbf{x_{i3}} \;\; \mathbf{x_{i3}'} \;\; \mathbf{x_{i+1}} \;\; \mathbf{x_{i+1}'}\right], \tag{28}$$

where $\mathbf{x_{ik}}' = \Delta t_i \mathbf{f}(t_{ik}, \mathbf{x_{ik}}, \mathbf{u_{ik}})$ and matrix B is given by:

$$B = \begin{bmatrix} 1 & 0 & 1 & 0 & 1 & 0 & 1 & 0 \\ 0 & 1 & \tau_{i2} & 1 & \tau_{i3} & 1 & 1 & 1 \\ 0 & 0 & \tau_{i2}^2 & 2\tau_{i2} & \tau_{i3}^2 & 2\tau_{i3} & 1 & 2 \\ 0 & 0 & \tau_{i2}^3 & 3\tau_{i2}^2 & \tau_{i3}^3 & 3\tau_{i3}^2 & 1 & 3 \\ 0 & 0 & \tau_{i2}^4 & 4\tau_{i2}^3 & \tau_{i3}^4 & 4\tau_{i3}^3 & 1 & 4 \\ 0 & 0 & \tau_{i2}^5 & 5\tau_{i2}^4 & \tau_{i3}^5 & 5\tau_{i3}^4 & 1 & 5 \\ 0 & 0 & \tau_{i2}^6 & 6\tau_{i2}^5 & \tau_{i3}^6 & 6\tau_{i3}^5 & 1 & 6 \\ 0 & 0 & \tau_{i2}^7 & 7\tau_{i2}^6 & \tau_{i3}^7 & 7\tau_{i3}^6 & 1 & 7 \end{bmatrix}. \tag{29}$$

If matrix A_i is known, the states can be interpolated at any given point on the i^{th} segment using Eq. 27. The control defines the sails normal direction $\hat{\mathbf{n}}_{SSF}(t)$ over each segment through the variables $\mathbf{u_i}$ and $\dot{\mathbf{u}}_\mathbf{i}$, and is modelled to vary semi-linearly over each segment and such that $|\hat{\mathbf{n}}_{SSF}(t)| = 1$:

$$\hat{\mathbf{n}}_{SSF}(t) = \mathbf{u}(t) = \frac{\mathbf{u_i} + (t - t_i)\dot{\mathbf{u}}_\mathbf{i}}{|\mathbf{u_i} + (t - t_i)\dot{\mathbf{u}}_\mathbf{i}|}. \tag{30}$$

B. Defect constraints

Although the polynomial in Fig. 7(b) describes the states over a segment, it does not automatically satisfy the dynamics. Therefore, at the three defect points $\mathbf{x_{i,1}}$, $\mathbf{x_{i,c}}$ and $\mathbf{x_{i,4}}$, the defect constraints are evaluated, forcing the polynomial to adhere to the dynamics. The defect constraints can be illustrated using Fig. 8.

The states at the defect points are found using [14]:

$$\mathbf{x_{i1}} = a_{i1}\mathbf{x_i} + a_{i21}\mathbf{x_{i2}} + a_{i31}\mathbf{x_{i3}} + a_{ip1}\mathbf{x_{i+1}} + \Delta t_i \left(v_{i1}\mathbf{f_i} + v_{i21}\mathbf{f_{i2}} + v_{i31}\mathbf{f_{i3}} + v_{ip1}\mathbf{f_{i+1}}\right), \tag{31}$$

$$\mathbf{x_{ic}} = a_{ic}\mathbf{x_i} + a_{i2c}\mathbf{x_{i2}} + a_{i3c}\mathbf{x_{i3}} + a_{ipc}\mathbf{x_{i+1}} + \Delta t_i \left(v_{ic}\mathbf{f_i} + v_{i2c}\mathbf{f_{i2}} + v_{i3c}\mathbf{f_{i3}} + v_{ipc}\mathbf{f_{i+1}}\right), \tag{32}$$

and

$$\mathbf{x_{i4}} = a_{i4}\mathbf{x_i} + a_{i24}\mathbf{x_{i2}} + a_{i34}\mathbf{x_{i3}} + a_{ip4}\mathbf{x_{i+1}} + \Delta t_i \left(v_{i4}\mathbf{f_i} + v_{i24}\mathbf{f_{i2}} + v_{i34}\mathbf{f_{i3}} + v_{ip4}\mathbf{f_{i+1}}\right), \tag{33}$$

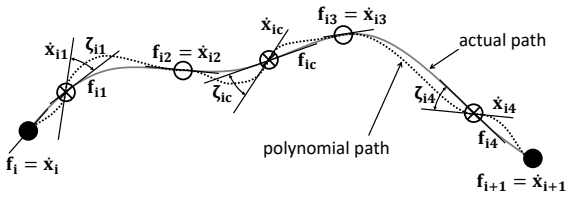

Fig. 8 Sketch containing a visualization of the defect constraints $\boldsymbol{\zeta_i}$. Adapted from Ref. [5].

where the required constants a and v are given in Table 4. Using the node, internal and defect points, the defect constraints $\boldsymbol{\zeta}$ are evaluated as [14]:

$$\boldsymbol{\zeta_{i1}} = b_{i1}\mathbf{x_i} + b_{i21}\mathbf{x_{i2}} + b_{i31}\mathbf{x_{i3}} + b_{ip1}\mathbf{x_{i+1}} + \Delta t_i \left(w_{i1}\mathbf{f_i} + w_{i11}\mathbf{f_{i1}} + w_{i21}\mathbf{f_{i2}} + w_{i31}\mathbf{f_{i3}} + w_{ip1}\mathbf{f_{i+1}}\right), \quad (34)$$

$$\boldsymbol{\zeta_{ic}} = b_{ic}\mathbf{x_i} + b_{i2c}\mathbf{x_{i2}} + b_{i31}\mathbf{x_{i3}} + b_{ipc}\mathbf{x_{i+1}} + \Delta t_i \left(w_{ic}\mathbf{f_i} + w_{i2c}\mathbf{f_{i2}} + w_{icc}\mathbf{f_{ic}} + w_{i3c}\mathbf{f_{i3}} + w_{ipc}\mathbf{f_{i+1}}\right) \quad (35)$$

and

$$\boldsymbol{\zeta_{i4}} = b_{i4}\mathbf{x_i} + b_{i24}\mathbf{x_{i2}} + b_{i34}\mathbf{x_{i3}} + b_{ip4}\mathbf{x_{i+1}} + \Delta t_i \left(w_{i4}\mathbf{f_i} + w_{i24}\mathbf{f_{i2}} + w_{i34}\mathbf{f_{i3}} + w_{i44}\mathbf{f_{i4}} + w_{ip4}\mathbf{f_{i+1}}\right), \quad (36)$$

where the constants b and w are also given in Table 4. If the value of $\boldsymbol{\zeta}$ is equal to zero, the dynamics over the polynomial are accurately approximated up to $O(\Delta t_i^{12})$ [5].

C. Path constraints

The defect constraints are used to comply with the dynamics of the system. For a feasible trajectory, it is also required to comply with path (in)equality constraints. As inequality constraints cannot be solved directly by NLP solvers [16], they are rewritten to introduce slack variables $\boldsymbol{\eta}$, transforming the inequality constraints in equality constraints [5]. The introduction of the slack variables enables the inequality constraint to be active at every node point. Although this requires the algorithm to always evaluate every constraint, it eliminates the need for determining the active-set of constraints.

Table 4 Constants used for determining defect points and defect constraints. [14, 15]

Constant	Value	Constant	Value
v_{i1}	2.57387738427162e-2	a_{i1}	6.18612232711785e-1
v_{i21}	-5.50098654524528e-2	a_{i21}	3.34253095933642e-1
v_{i31}	-1.53026046503702e-2	a_{i31}	1.52679626438851e-2
v_{ip1}	-2.38759243962924e-3	a_{ip1}	3.18667087106879e-2
v_{ic}	9.92317607754556e-3	a_{ic}	1.41445282326366e-1
v_{i2c}	9.62835932121973e-2	a_{i2c}	3.58554717673634e-1
v_{i3c}	-9.62835932121973e-2	a_{i3c}	3.58554717673634e-1
v_{ipc}	-9.92317607754556e-3	a_{ipc}	1.41445282326366e-1
v_{i4}	2.38759243962924e-3	a_{i4}	3.18667087106879e-2
v_{i24}	1.53026046503702e-2	a_{i24}	1.52679626438851e-2
v_{i34}	5.50098654524528e-2	a_{i34}	3.34253095933642e-1
v_{ip4}	-2.57387738427162e-2	a_{ip4}	6.18612232711785e-1
w_{i1}	1.62213410652341e-2	b_{i1}	8.84260109348311e-1
w_{i11}	1.38413023680783e-1	-	-
w_{i21}	9.71662045547156e-2	b_{i21}	-8.23622559094327e-1
w_{i31}	1.85682012187242e-2	b_{i31}	-2.35465327970606e-2
w_{ip1}	2.74945307600086e-3	b_{ip1}	-3.70910174569208e-2
w_{ic}	4.83872966828888e-3	b_{ic}	7.86488731947674e-2
w_{i2c}	1.00138284831491e-1	b_{i2c}	8.00076026297266e-1
w_{icc}	2.43809523809524e-1	-	-
w_{i3c}	1.00138284831491e-1	b_{i3c}	-8.00076026297266e-1
w_{ipc}	4.83872966828888e-3	b_{ipc}	-7.86488731947674e-2
w_{i4}	2.74945307600086e-3	b_{i4}	3.70910174569208e-2
w_{i24}	1.85682012187242e-2	b_{i24}	2.35465327970606e-2
w_{i34}	9.71662045547156e-2	b_{i34}	8.23622559094327e-1
w_{i44}	1.38413023680783e-1	-	-
w_{ip4}	1.62213410652341e-2	b_{ip4}	-8.84260109348311e-1

1. Path constraints on the control vector

The control, $\mathbf{u}(t) = \hat{\mathbf{n}}_{SSF}(t)$ is described by a Cartesian unit vector. As the cone angle is allowed to vary only between 0 and 90 deg, the $u_{ix,SSF}$ element needs to be constrained to be larger than zero:

$$g_{i1} = u_{ix,SSF} - \eta_{i1}^2. \tag{37}$$

The corresponding slack variable η_{i1} should thus equal $\sqrt{u_{ix,SSF}}$. If u_{ix} becomes smaller than zero, the constraint in Eq. 37 will always be violated for any real η_{i1}, and thus the constraint ensures $u_{ix} \geq 0$.

As the control describes an unit vector, it is also required for the norm of the control to be equal to 1; $|\mathbf{u_i}| = 1$, which can be expressed into a path constraint as:

$$g_{i2} = 1 - \sqrt{u_{ix,SSF}^2 + u_{iy,SSF}^2 + u_{iz,SSF}^2}. \tag{38}$$

Finally, three control continuity constraints across the segments are included, which ensures that the control over the trajectory is described by a piecewise linear function:

$$g_{i3} = u_{ix,SSF} + \dot{u}_{ix,SSF}\Delta t_i - u_{i+1,x,SSF}, \tag{39}$$

$$g_{i4} = u_{iy,SSF} + \dot{u}_{iy,SSF}\Delta t_i - u_{i+1,y,SSF} \tag{40}$$

and

$$g_{i5} = u_{iz,SSF} + \dot{u}_{iz,SSF}\Delta t_i - u_{i+1,z,SSF}. \tag{41}$$

2. Path constraints altitude

In order to avoid impact and numerical integration issues during flybys, altitude constraints are introduced. First of all, a minimum altitude with respect to Earth is enforced of $h_{31,min} = 10\,000$ km. Similarly the minimum altitude with respect to the Moon is set equal to four Moon radii or $h_{32,min} = 6952$ km. The minimum altitude constraints are scaled to dimensionless units and rewritten to equality constraints through the slack variables η_{i2} and η_{i3} resulting in:

$$g_{i6} = R_e + h_{31,min} - r_{i31} + \eta_{i2}^2, \tag{42}$$

and

$$g_{i7} = R_m + h_{32,min} - r_{i32} + \eta_{i3}^2. \tag{43}$$

3. Path constraint on sail rotation rate

Finally, the maximum allowable rotation rate of the sail is constrained. A solar sail is a flexible structure with a large moment of inertia. Rapid changes in attitude are therefore not feasible for large sails. Therefore the maximum rotation rate of the solar sail with respect to the Sun-sail line is constrained to $\dot{u}_{max} = 20\,\text{deg/day}$. If $\Delta\phi_i$ is a rotation of the solar sail over segment i, it can be assumed that $\Delta\phi_i/\Delta t_i \approx |\dot{\mathbf{u}}|$ for small Δt_i. By converting the 20 deg/day to dimensionless units, the rotation rate constraint is enforced in the form:

$$g_{i8} = 0.01\left(\dot{u}_{max} - \sqrt{\dot{u}_{ix,SSF}^2 + \dot{u}_{iy,SSF}^2 + \dot{u}_{iz,SSF}^2} - \eta_{i4}^2\right), \tag{44}$$

where the constraint is scaled by a factor 0.01 to improve convergence of the NLP-solver.

As can be seen, a total of eight path constraints are active at each node point. In addition to the path constraints, point constraints must be added to the trajectory.

D. Point constraints

The defect and path constraints allow for the construction of feasible trajectories. In order to find feasible trajectories that are actually connected to the SSO, nine point constraints are added on the final node to ensure that the final states and controls comply with the SSO.

$$\mathbf{c_n} = \begin{bmatrix} \mathbf{x_n} \\ \mathbf{u_n} \end{bmatrix} - \begin{bmatrix} \mathbf{x_{SSPO}}(t_n) \\ \mathbf{u_{SSPO}}(t_n) \end{bmatrix} \tag{45}$$

In addition, point constraints are added on the departure node, such that the trajectory departs from GEO-altitude, $r_{GEO} = 35\,786\,\text{km}$, and from a parking orbit that coincides with a Soyuz HEO:

$$\mathbf{c_1} = \begin{bmatrix} \sqrt{(x_{1,SYN} + \mu)^2 + y_{1,SYN}^2 + z_{1,SYN}^2} \\ i_{ECI} \\ \omega_{ECI} \end{bmatrix} - \begin{bmatrix} r_{GEO}/U_{length} \\ i_{HEO} \\ \omega_{HEO} \end{bmatrix}, \tag{46}$$

where the two-body inclination and argument of perigee are determined in the ECI frame using the equations in subsection III B.

E. The Gauss-Newton algorithm

In order to solve the trajectory problem, the states and constraints are rewritten as an NLP problem. Let the decision variables for a single segment be collected in a decision vector $\mathbf{X_i}$ of size 28×1:

$$\mathbf{X_i} = \begin{bmatrix} \mathbf{x_i}^T & \mathbf{u_i}^T & \dot{\mathbf{u}}_\mathbf{i}^T & \mathbf{x_{i,2}}^T & \mathbf{x_{i,3}}^T & \boldsymbol{\eta}_\mathbf{i}^T \end{bmatrix}^T, \tag{47}$$

subjected to the 26×1 constraint vector:

$$\mathbf{F_i} = \begin{bmatrix} \boldsymbol{\zeta_{i1}}^T & \boldsymbol{\zeta_{ic}}^T & \boldsymbol{\zeta_{i4}}^T & \mathbf{g_i}^T \end{bmatrix}^T. \tag{48}$$

For all segments, the decision vector becomes:

$$\mathbf{X} = \begin{bmatrix} \mathbf{X_1}^T & \mathbf{X_2}^T & \dots & \mathbf{X_{n-2}}^T & \mathbf{X_{n-1}}^T & \mathbf{x_n}^T & \mathbf{u_n}^T \end{bmatrix}^T, \tag{49}$$

with the corresponding constraint vector:

$$\mathbf{F} = \begin{bmatrix} \mathbf{c_1}^T & \mathbf{F_1}^T & \mathbf{F_2}^T & \dots & \mathbf{F_{n-2}}^T & \mathbf{F_{n-1}}^T & \mathbf{c_n}^T \end{bmatrix}^T. \tag{50}$$

For a trajectory consisting of n segments, a total of $28(n-1)+9$ decision variables are used to satisfy $26(n-1)+12$ constraints. For a trajectory of 50 nodes, this would result in 1381 variables subject to 1286 constraints, which would be excessively large to solve using grid searches, Monte-Carlo methods or genetic algorithms. Since all constraints are smooth and differentiable, the Gauss-Newton algorithm is used to find decision vector $\mathbf{X}$ for which $\mathbf{F} = \mathbf{0}$ [5]. The Gauss-Newton algorithm minimizes the sum of squared constraint violations, converges quadratically [18] and does not require the computation of second order derivatives. Although there are an infinite number of search directions $D\mathbf{X}$ which satisfy:

$$\mathbf{F}(\mathbf{X}) = \frac{\partial \mathbf{F}(\mathbf{X})}{\partial \mathbf{X}} \cdot D\mathbf{X}, \tag{51}$$

the Gauss-Newton algorithm solves for the minimum norm value of $D\mathbf{X}$, such that the characteristics of the initial guess are best preserved [18]. Since the initial guess is a locally optimal solution with respect to increasing the spacecraft's energy, it is indeed desired to find a feasible trajectory close to the initial guess.

First the derivative of the constraint vector $\mathbf{F}$ with respect to $\mathbf{X}$ is calculated, resulting in the Jacobi matrix ($D\mathbf{F} = \frac{\partial \mathbf{F}(\mathbf{X})}{\partial \mathbf{X}}$). Note that $\mathbf{F_i}$ is only dependent on $\mathbf{X_i}$, $\mathbf{x_{i+1}}$ and $\mathbf{u_{i+1}}$. Similarly, the point constraints $\mathbf{c_1}$ and $\mathbf{c_n}$ are only dependent on the departure and arrival node. In order to calculate $D\mathbf{F}$ efficiently, only the relevant derivatives have to be evaluated, while the other derivatives are known a priori to be equal to zero.

The efficient calculation of the derivatives is achieved by using the complex step method, which gives an accuracy similar to that of the central step method, with only a single function evaluation [24]. The j^{th} column of $D\mathbf{F_i}$ can be calculated by adding a small imaginary number to the j^{th} element of vector $\mathbf{X_i}$ and evaluating $\mathbf{F_i}$ using the complex step method:

$$\frac{\partial \mathbf{F_i}}{\partial X_{ij}} = \frac{Imag\left(\mathbf{F_i}\left(\left[X_{i1} \;\; \ldots \;\; X_{i(j-1)} \;\; X_{ij} + \epsilon\sqrt{-1} \;\; X_{i(j+1)} \;\; \ldots \;\; X_{i28} \;\; \mathbf{x_{i+1}}^T \;\; \mathbf{u_{i+1}}^T\right]^T\right)\right)}{\epsilon}, \quad (52)$$

where the partial Jacobi matrix $\frac{\partial \mathbf{F_i}}{\partial \mathbf{X_i}}$ has size 26×19 and ϵ is a small constant of value 10^{-10}. Note that the partial derivatives $\frac{\partial \mathbf{F_i}}{\partial \mathbf{x_{i+1}}}$, $\frac{\partial \mathbf{F_i}}{\partial \mathbf{u_{i+1}}}$, $\frac{\partial \mathbf{c_1}}{\partial \mathbf{X_1}}$, $\frac{\partial \mathbf{c_n}}{\partial \mathbf{x_n}}$ and $\frac{\partial \mathbf{c_n}}{\partial \mathbf{u_n}}$ also need to be evaluated. The structure containing the non-zero elements of the complete Jacobi matrix using seven nodes is shown in Fig. 9.

The Jacobi matrix is applied in the Gauss-Newton algorithm to determine the search direction $D\mathbf{X}$ [5]:

$$D\mathbf{X} = -D\mathbf{F}(\mathbf{X})\left(\left[D\mathbf{F}(\mathbf{X}) \cdot D\mathbf{F}(\mathbf{X})^T\right]^{-1}\mathbf{F}(\mathbf{X})\right). \quad (53)$$

Note that if $n = 50$, the matrix $D\mathbf{F}$ has dimensions 1234×1381, containing just 26959 (1.582%) non-zero elements, which can be efficiently stored using MATLAB®'s "sparse.m" function. Furthermore, the matrix multiplications and inverses of $D\mathbf{F}$ are efficiently calculated using the unsymmetric multifrontal method provided by UMFPACK [25].

The found search direction varies in quality due to nonlinear changes in the dynamics or constraints, especially if the initial guess is far away from a solution or if close flybys around the Earth or Moon are present. In order to improve the radius of convergence, a line search algorithm is used in the form [16]:

$$\mathbf{X_{new}} = \mathbf{X} + \alpha_{ls} D\mathbf{X}, \quad (54)$$

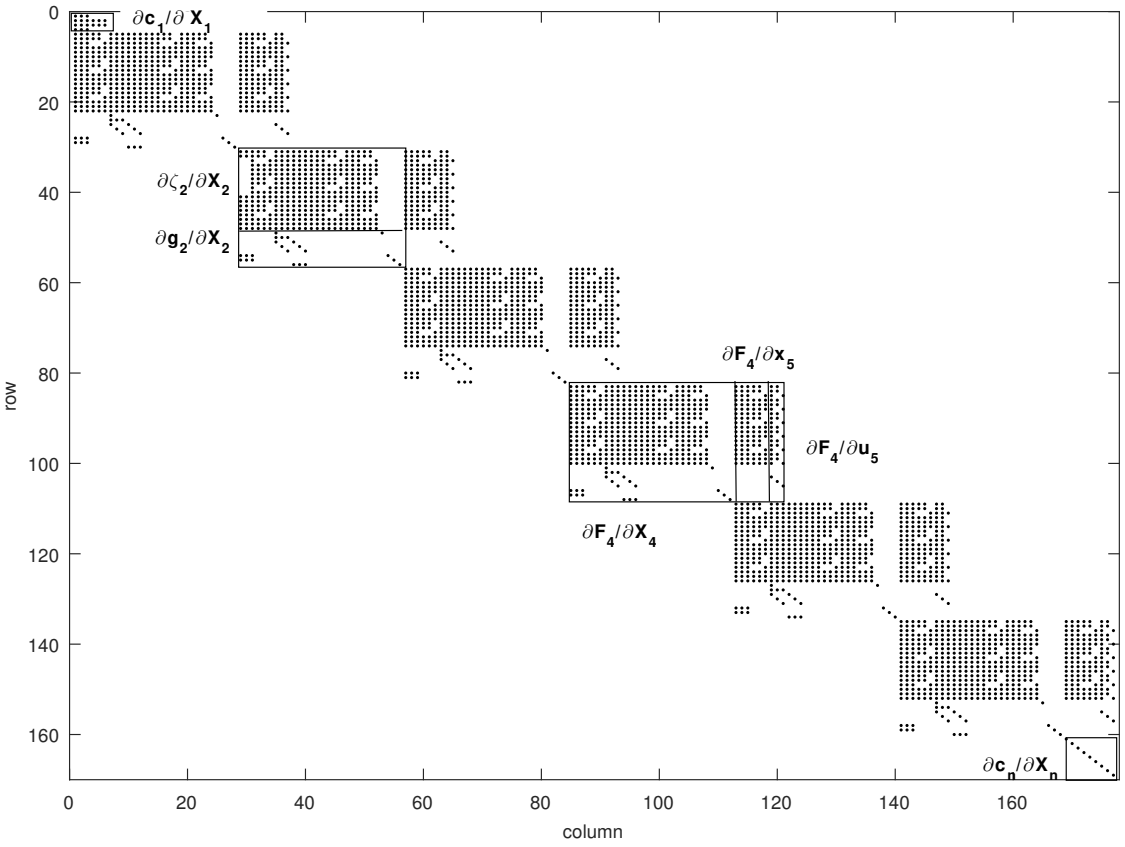

Fig. 9 Structure of nonzero elements of the Jacobi matrix ($D\mathbf{F}$) for a trajectory problem with six segments and seven nodes.

where α_{ls} is a parameter with a value selected between 0.1 and 1.0 that minimizes $\sum \mathbf{F}(\mathbf{X}+\alpha_{ls} D\mathbf{X})$. If the search direction points in an unfeasible direction, the linesearch algorithm multiplies the search direction with a small number, resulting in a new estimate of $\mathbf{X_{new}}$. From this new point, a new and potentially better search direction can be found. This procedure is repeated untill are constraints are satisfied up to $O(10^{-10})$.

VI. Mesh and error control

Although the 12^{th}-order Gauss-Lobatto method is highly accurate, an discretization error is made across every segment, which can become unbounded during approaches of the Earth or Moon. In order to decrease the discretization error over the trajectory, the number of linear spaced nodes can be increased, but this would increase the computation time. A more efficient method is to estimate the error made over each segment and adjust the mesh spacing accordingly. An optimal mesh

distributes the nodes such that the error over each segment is constant. The piecewise polynomials have degree seven, for which the error over the i^{th} segment can be approximated using:

$$e_i = C\Delta t_i^8 ||\mathbf{x}_i^{(8)}|| + O(\Delta t_i^9) \tag{55}$$

where C is a dimensionless constant equal to $2.935\,793\,951\,418\,95 \times 10^{-9}$ [26] and $\mathbf{x}^{(8)}$ is the eight-order derivative of the state vector. Since $\mathbf{x}$ is described by a seventh-degree polynomial in Eq. 27, the eight-order derivative is unknown. However, it can be approximated by applying a difference formula in order to evaluate $\mathbf{x}^{(8)}$ over multiple segments [17]:

$$||\mathbf{x}^{(8)}|| \approx \theta_8(t) = \max \left[2\tfrac{|\mathbf{y}_1 - \mathbf{y}_2|}{\Delta t_1 + \Delta t_2} \right] \text{over } (t_1, t_2) \tag{56}$$

$$||\mathbf{x}^{(8)}|| \approx \theta_8(t) = \max \left[\tfrac{|\mathbf{y_{i-1}} - \mathbf{y_i}|}{\Delta t_{i-1} + \Delta t_i} + \tfrac{|\mathbf{y_{i+1}} - \mathbf{y_{i+2}}|}{\Delta t_{i+1} + \Delta t_{i+2}} \right] \text{over } (t_i, t_{i+1}) \tag{57}$$

$$||\mathbf{x}^{(8)}|| \approx \theta_8(t) = \max \left[2\tfrac{|\mathbf{y}_{n-2} - \mathbf{y}_{n-1}|}{\Delta t_{n-2} + \Delta t_{n-1}} \right] \text{over } (t_{n-2}, t_{n-1}) \tag{58}$$

where $\mathbf{y_i}$ is the dimensionless seventh order derivative on segment i, given by:

$$\mathbf{y_i} = \frac{\mathbf{x}^{(7)}(\tau)}{\Delta t_i} = 7\,! \left[\mathbf{x_i} \;\; \mathbf{x'_i} \;\; \mathbf{x_{i2}} \;\; \mathbf{x'_{i2}} \;\; \mathbf{x_{i3}} \;\; \mathbf{x'_{i3}} \;\; \mathbf{x_{i+1}} \;\; \mathbf{x'_{i+1}} \right] \cdot \frac{\mathbf{b}}{\Delta t_i^7}, \tag{59}$$

in which $\mathbf{b}$ is the last column of B^{-1}. The new mesh points can now be computed using [5]:

$$t_{i+1} = I(t_{i+1})^{-1} \left[\tfrac{iI(t_n)}{n-1} \right] \tag{60}$$

where

$$I(t) = \int_{t_1}^{t} \theta_8(s)^{1/8} ds. \tag{61}$$

Since $\theta_8(t)$ is a piecewise constant function, the integral $I(t)$ is a piecewise linear function, which can be solved for t_{i+1} in Eq. 60. Using the new mesh, the states are interpolated using Eq. 27, such that the dynamics are conserved. Similarly, the control and control derivative are also interpolated. Finally, the slack variables ($\boldsymbol{\eta}$) are recalculated for the new controls and states, such that the path constraint violation of the new mesh is minimized.

Note that the activation of the solar sail after the one-day ballistic phase generates a discontinuity in the dynamics. Therefore, the trajectory before activation and the trajectory after activation of the solar sail are treated as different phases in the error estimation algorithm. As a result, the moment at which the solar sail is activated, always coincides with a node point.

VII. Design process

In order to generate feasible transfer trajectories, the theory described in the previous sections is applied in a systematical manner. First, an initial guess to the trajectory optimization problem is generated. Secondly, the departure altitude as well as the perigee altitude of the HEO orbit are reduced using a stepwise approach. If a transfer trajectory with a perigee altitude of 250 km is found, the parking orbit inclination and argument of perigee constraints are enforced. Subsequently, the found trajectory for SC1 is used as an initial guess for the trajectory problem of SC2. Finally, a subsystem mass analysis is carried out for the fastest trajectories.

A. Generating the initial guess

To generate an initial guess for SC1, first a fixed arrival time ($t_{arrival}$) on the SSO is selected. To find the corresponding state, $\mathbf{x_{SSO}}$, the states are integrated along the SSO from $t = 0$ to $t_{arrival}$ using MATLAB®'s "ode45.m" function [27] in accordance with subsection III A. An initial guess for the transfer trajectory is subsequently generated by propagating the dynamics of the CR3BP from $\mathbf{x_{SSO}}$ in reverse time, where the LOSL is used to determine the control along the trajectory. The backwards propagated trajectory is truncated in the interval $\left[t_{arrival} \;\; t_{arrival} - \Delta t_{transfer,max}\right]$ at the point with the closest approach to GEO-altitude. Here $\Delta t_{transfer,max}$ is the maximum allowable transfer time. The trajectory is rewritten as the NLP problem described in section V, by evaluating the states, controls, rotation rates and slack variables on the node and internal points. In total, 100 equally spaced node points per lunar period are used to describe the initial guess. A flowchart for generating the initial guess appears in Figure 10.

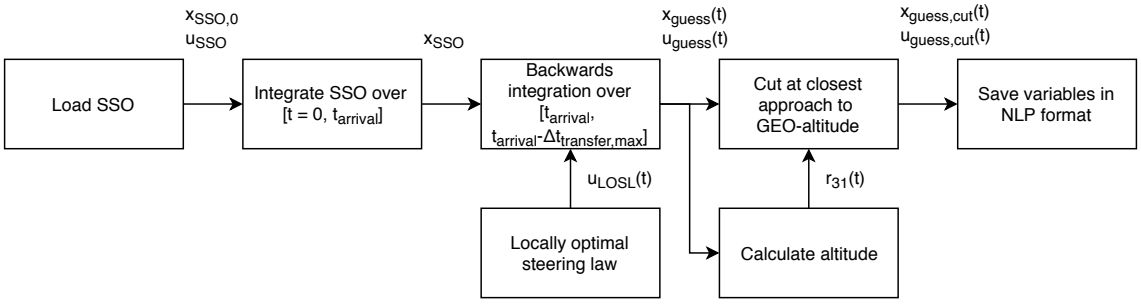

Fig. 10 Flowchart used for generating the initial guess using the LOSL

B. Enforcing altitude constraints

In order to increase the feasibility of the trajectory, constraints are enforced through the collocation method. In addition to the constraints, the sail acceleration is set to zero during the first day of the trajectory, allowing enough time for the solar sail to deploy. The approach in Fig. 10 does not ensure that the start of the trajectory occurs at GEO-altitude. Therefore, the altitude constraint on the departure point is gradually introduced, reducing the altitude of the departure point to GEO-altitude using ten consecutive steps. During each step, the constraints in the NLP problem are enforced using the Gauss-Newton algorithm, followed by a new mesh refinement with an equidistributed error. Such a stepwise approach is applied as the initial guess may be far from a constraint-satisfying solution and the NLP-solver might diverge for such large constraint violations. Furthermore, intermediate mesh refinements will improve the convergence to a feasible solution. When the departure point coincides with GEO-altitude, the orbital elements of the parking orbit corresponding to the departure point are calculated. The GEO-altitude constraint is then replaced by the perigee altitude constraint and is reduced in a similar stepwise approach to 250 km using 20 steps. During the perigee reduction steps, no altitude constraint on the departure point is enforced. The altitude of the departure point might therefore depart from GEO-altitude and thus, the trajectory is trimmed by cutting or propagating the starting point up to GEO-altitude. This allows for small variations in the overall transfer time during each iteration and enables a wider radius of convergence. The flowchart for enforcing the GEO-altitude and perigee altitude constraints is shown in Fig. 11.

C. Trajectory for SC1

If a trajectory is found with a perigee altitude of 250 km and a departure altitude equal to GEO altitude, additional constraints are enforced, such that the trajectory coincides with a HEO of the Soyuz launcher described in section III B. An inclination constraint of 6 deg as well as an argument of perigee constraint of 178 deg are enforced in a single step. Note that, in order to complete the transformation between the ECL and SYN frames, a phase angle $\varphi_{2,0}$ in Eq. 17 is selected through a grid search, for which the discrepancy with respect to the newly enforced constraints is minimal.

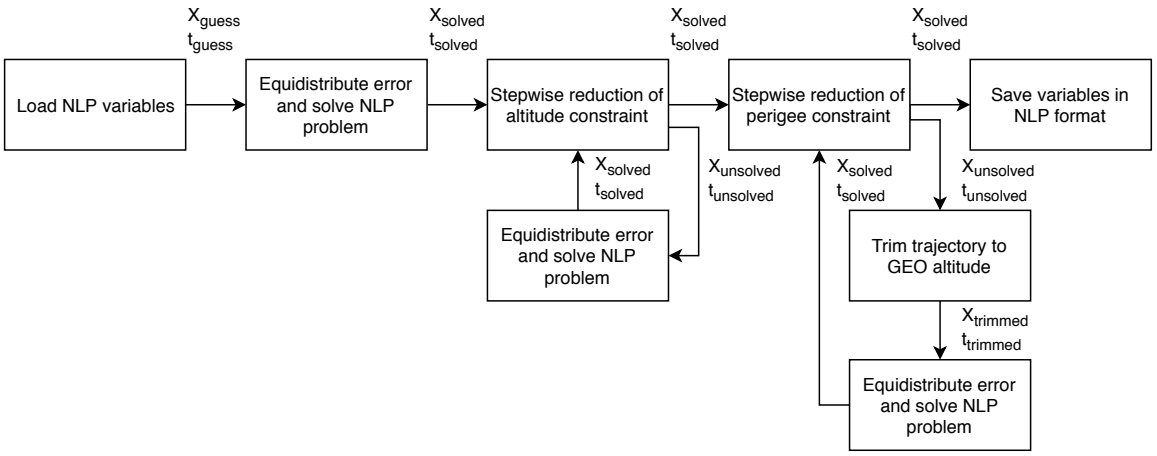

Fig. 11 Flowchart used for enforcing the GEO-altitude and perigee altitude constraints using a stepwise approach

D. Trajectory for SC2

Once a feasible trajectory for SC1 is found, a second trajectory is sought for SC2. Preferably, both spacecraft are launched at the same time with the same launcher, reducing mission cost and complexity. This requires two distinct transfer trajectories with different arrival points along the SSO, but with identical departure conditions. It is difficult to exactly match six states at a set departure time, even using the collocation method described in this work. Therefore the following method is adapted. It appears that the transfer trajectories and departure conditions remain close to the Earth-Moon orbital plane. In addition, the SSOs of the two spacecraft are close to symmetrical in the $(\hat{\mathbf{x}}_{SYN}, \hat{\mathbf{y}}_{SYN})$-plane. The found trajectory for SC1 can therefore be mirrored in the $(\hat{\mathbf{x}}_{SYN}, \hat{\mathbf{y}}_{SYN})$-plane and used as an initial guess for SC2. This results in a feasible trajectory satisfying the dynamics and path constraints, but with minor constraint violations on the departure point and major constraint violations at the arrival point. Furthermore, since the entire trajectory is mirrored, the arrival control, $n_{z,SSF}$, is pitched in the opposite direction with respect to the desired SSO attitude. Also, the SSO is not perfectly symmetric in the $(\hat{\mathbf{x}}_{SYN}, \hat{\mathbf{y}}_{SYN})$-plane, which causes a small offset between the final node and the SSO. In order to reduce the constraint violations, an additional trajectory phase is added at the end of the transfer to allow the control to reverse its z-component. As an initial guess for this phase, the states of the SSO are used over which the control varies semi-linear from $\hat{\mathbf{n}}_{SC2,SSF},(t_{f,SC1}) = \begin{bmatrix}\cos\alpha & 0 & \sin\alpha\end{bmatrix}^T$ to $\hat{\mathbf{n}}_{SC2,SSF}(t_{f,SC2}) = \begin{bmatrix}\cos\alpha & 0 & -\sin\alpha\end{bmatrix}^T$

in accordance with Eq. 30, with $\alpha = 35.26\,\text{deg}$ as in section III A. A total of 50 nodes are used to describe this phase, with a time length of π/Ω_s or $0.25P_{SSO}$, which equals 14.84 days. The flowchart used for enforcing parking orbit constraints for SC1 and finding the trajectory with identical launch conditions for SC2 can be seen in Fig. 12.

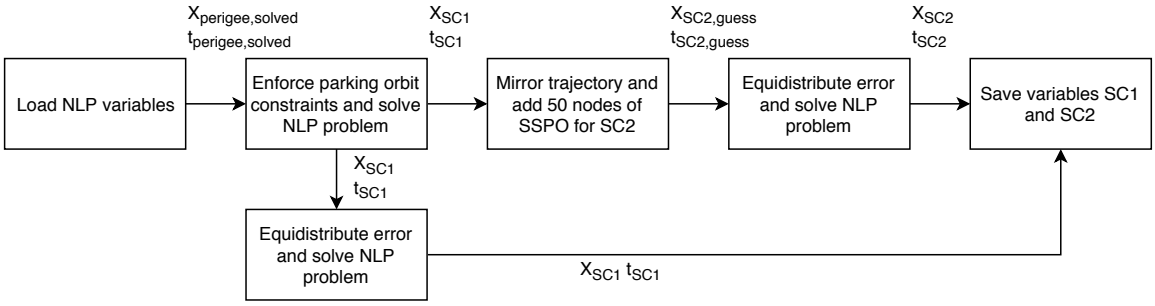

Fig. 12 Flowchart used for enforcing the parking orbit constraints for SC1 and finding a feasible trajectory for SC2.

E. Spacecraft mass budget

A preliminary spacecraft mass budget is investigated for the set of trajectories for SC1 and SC2 with the shortest transfer time. Two scenario's are presented. The first scenario considers the mass breakdown for a large satellite, utilizing the complete payload capacity of a single Soyuz launch. The second scenario considers a cubesat demonstration mission, with an assumed spacecraft mass of 10 kg. A parametric mass analysis is carried out to find an estimation of the subsystem masses. As solar-sail technology is relatively new, no reliable mass estimation can be made based on reference satellites. Instead mass fractions for communication satellites are used from Ref. [28], where the mass fraction used for the propulsion subsystem is replaced by a calculation of the required sail area and consequently the required sail mass. The used mass fractions are shown in Table 5.

The solar-sail mass can be calculated as a function of the solar-sail area A_s using the critical sail loading σ_s of $1.53\,\text{g/m}^2$ [1] and the lightness number β_0:

$$\beta_0 = \sigma^* \frac{A_s}{m_3} = \frac{a_{EM} r_4^2}{\mu_4}, \tag{62}$$

where r_4 is the distance to the Sun equal to 149.6×10^6 km [20] and μ_4 is the gravitational parameter of the Sun equal to $132\,712 \times 10^6\,\text{km}^3/\text{s}^2$ [20]. Using these values and an a_{EM} equal to $0.2698\,\text{mm/s}^2$

Table 5 Mass fractions for communication satellites from Ref. [28]. Normalized mass fractions found by removing the propulsion subsystem.

	Mass fractions						
	Payload	Structure	Thermal	Power	TT&C	ADCS	Propulsion
Fractions	0.274	0.213	0.036	0.319	0.048	0.069	0.038
Normalized fractions	0.2857	0.221	0.0375	0.3326	0.0501	0.0719	-

it is found that β_0 equals 0.0455. The spacecraft mass m_3 is extracted from Fig. 5 and is used to determine the required sail area. The solar-sail mass can then be calculated using:

$$m_s = A_s \sigma_s \tag{63}$$

where the sail loading σ_s is equal to $0.010\,\mathrm{kg/m^2}$, which is assumed feasible for near-term sail technology [29].

VIII. Results

This section presents the results of the approach outlined in section VII. First, the trajectories created with the LOSL are presented. Subsequently, suitable trajectories are selected from this set, which are used as an initial guess for the collocation scheme. The results are initially presented without the rotation rate constraint active, followed by results that assumes a maximum rotation rate of $20\,\mathrm{deg/day}$. Finally the results of a subsystem mass analysis are presented for the trajectory with the shortest transfer time.

A. Trajectories with the LOSL

In order to generate a complete map of possible initial guess transfers, 2000 trajectories are generated using the reserve time LOSL propagation approach, by varying the arrival location along the SSO. A subset of 200 trajectories propagated for 12 days is shown in Fig. 13. It can be seen that the trajectories are not symmetric, due to the clockwise motion of the Sun, and thus the SRP direction. If the spacecraft is placed along one of these trajectories and applies the LOSL, it will arrive at the targeted SSO.

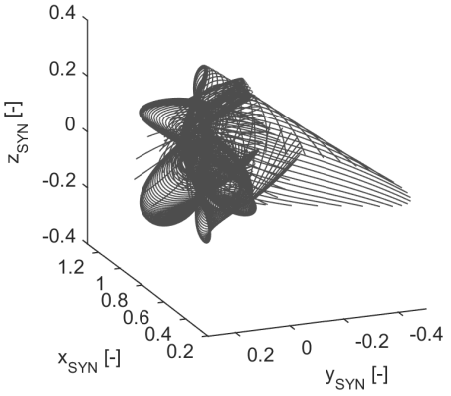

Fig. 13 Set of 200 trajectories connected to the SSO, propagated for twelve days.

By extending the propagation time to 365 days, the results in Fig. 14 are obtained. In Fig. 14, the distance of 2000 trajectories with respect to Earth is shown as a function of the arrival time on the SSO, expressed in orbital periods (P_{SSO}), and the transfer time.

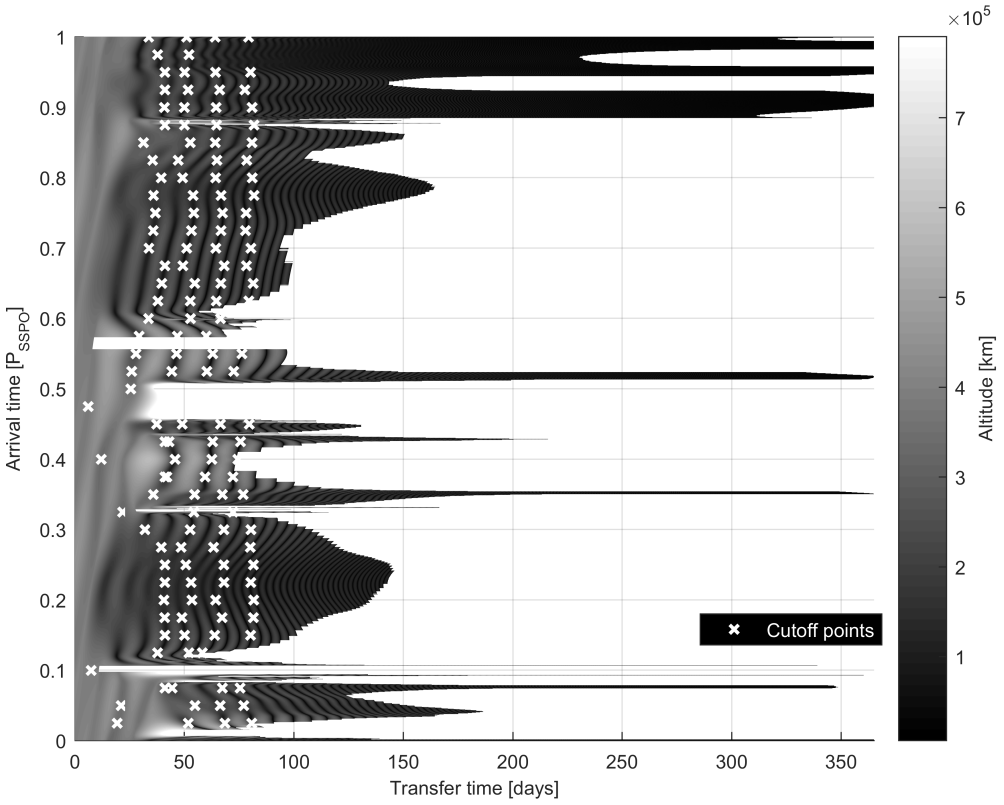

Fig. 14 Distance as a function of the arrival time on the SSO and transfer time to the SSO, including the cutoff points for the initial guesses of the collocation method.

In Fig. 14, the grayscale indicates that the trajectory starts at a large distance from Earth. Over the reverse time propagation, the trajectory will start to decrease its distance with respect to Earth, which is shown by the darker shaded areas. The propagation is terminated when the perigee altitude becomes less than 250 km, if the altitude reaches two Earth-Moon distances or if the solar sail crashes into the Moon. In most cases, the spacecraft will ultimately enter a spiral trajectory around Earth until a perigee altitude of 250 km is reached. The geometry of the trajectory varies significantly by changing the arrival location along the SSO. The quickest trajectory that reaches a perigee altitude of 250 km departs at $0.1205P_{SSO}$ and achieves a transfer time of 50.7 days. On the other hand, if an arrival time in the range of $0.890P_{SSO} - 1P_{SSO}$ is selected, trajectories are found containing a lengthy Earth escape spiral connected to a parking orbit similar to geostationary transfer orbit. A trajectory that arrives between $0.456P_{SSO} - 0.507P_{SSO}$ travels past the L_2 point and escapes the Earth-Moon system, while a trajectory arriving between $0.556P_{SSO} - 0.573P_{SSO}$ crashes into the Moon.

An example trajectory for $0.35P_{SSO}$ is shown in Fig. 15(a), with the corresponding control in Fig. 15(b). It can be seen that this trajectory departs from an highly elliptic orbit around Earth and performs multiple flybys close to the Earth. After a total transfer time of 108.88 days, the spacecraft arrives at the SSO. Furthermore, the rapid changes in the Cartesian components of the control in Fig. 15(b) require an extremely agile solar sail.

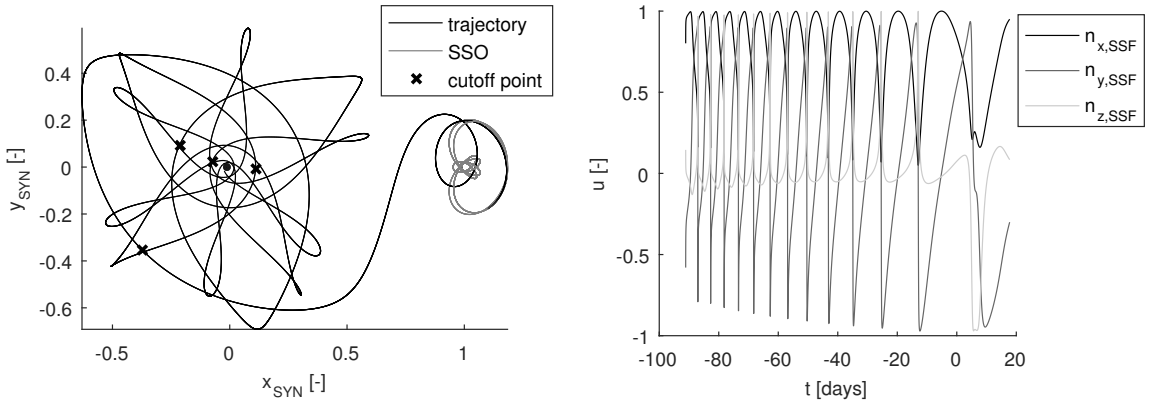

(a) (b)

Fig. 15 a) Transfer trajectory using locally optimal steering law for $t_{arrival} = 1.4\pi/\Omega_s = 0.35P_{SSO}$. b) Corresponding sail attitude.

While for the transfers that are truncated at an Earth altitude of 250 km match the required perigee altitude of the Soyuz parking orbits, the required inclination and argument of perigee of the HEO are currently unaccounted for. Furthermore, although the control is locally optimal, it can not be concluded that the global trajectory is optimal. Especially the lengthy Earth escape spirals contain multiple flybys at altitudes lower than 1000 km, which is not considered feasible for solar sails [30]. Also, the control provided by the LOSL contains singularities in attitude, which is not feasible with current or near-term technology [31]. Finally, the arrival attitude of the sail does not match the required attitude for the SSO. In order to address these discrepancies and improve the feasibility of the results, the collocation method of section V is employed.

B. Inactive rotation rate constraint

The initial guesses for the 12^{th}-order Gauss-Lobatto collocation method are extracted from the trajectories in Fig. 14. A maximum transfer time interval of 3π to 6π is imposed with steps of π, on which the closest flyby with respect to GEO is selected as cutoff point, as shown in Fig. 14 by the white crosses. The arrival time on the SSO is furthermore discretized using 40 points equally spaced along the SSO, i.e., at intervals of $0.1\pi/\Omega_s$ in dimensionless units. This results in 160 possible initial guesses that are subsequently transferred into the collocation method, where the performance of all resulting trajectories is shown in Fig. 16. On the x-axis, the transfer time of the trajectory is shown, while on the y-axis the apogee altitude of the corresponding HEO can be seen. If the apogee altitude of the parking orbit increases, the maximum deliverable spacecraft mass of a Soyuz launch to such orbit decreases as given in Fig. 5. Furthermore, the marker color describes the arrival time on the SSO and thus the used geometry for the initial guess. If a feasible trajectory with a perigee altitude of 250 km is found, it is shown as a circle in Fig. 16. In addition, converged trajectories with the desirable inclination and argument of perigee are indicated with a triangle symbol. Finally, if a feasible trajectory for SC2 is found, it is shown as a star in Fig. 16.

Out of 160 initial guesses only 36 transfers are found for which the perigee altitude constraint is satisfied. Other initial guesses failed to converge while reducing the altitude constraint using the stepwise approach. The quickest feasible trajectory requires a transfer time of 39.6 days and arrives

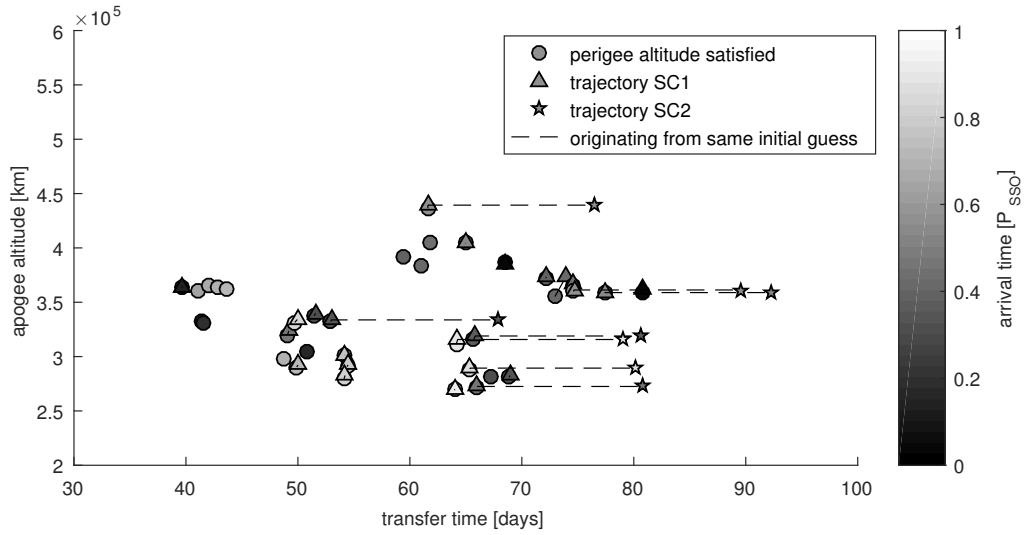

Fig. 16 Feasible transfer trajectories without rotation rate constraint active.

at the SSO at $0.125P_{SSO}$. After constraining the inclination and argument of perigee, 24 feasible trajectories remain, of which many have a close overlap between the round and triangular markers indicating that the perigee-altitude satisfying trajectories were already close to matching with a Soyuz HEO. Finally, the 8 trajectories for SC2 are represented by the star-shaped markers. Note that after SC2 arrives in proximity of the SSO, an additional period of π/Ω_s is added, which results in a constant increase in the transfer time of 14.84 days for SC2. The quickest trajectory for SC2 completes the transfer in 67.8 days, while the trajectory for SC1 with identical departure conditions arrives at the SSO in 53.0 days. These trajectories are shown in Fig. 17 with respect to the SYN frame, where the corresponding control as a function of time is given in Fig. 18.

Both trajectories follow the same path during the initial ballistic phase. After one day, the solar sail deploys and the two trajectories as well as the control history start to diverge. Over time, two flybys close to the Earth are performed at altitudes higher than 10 000 km. A major difference between the trajectories can be seen by comparing the arrival conditions in Fig. 17(c) and 17(d), as both spacecraft are connected to different points along the SSO. The control for both spacecraft is given in Fig. 18, which depicts an initial ballistic phase, followed by a rapidly varying control profile since no rotation rate is enforced. The results show that solar-sail transfer trajectories are possible, although the control still contains singularities.

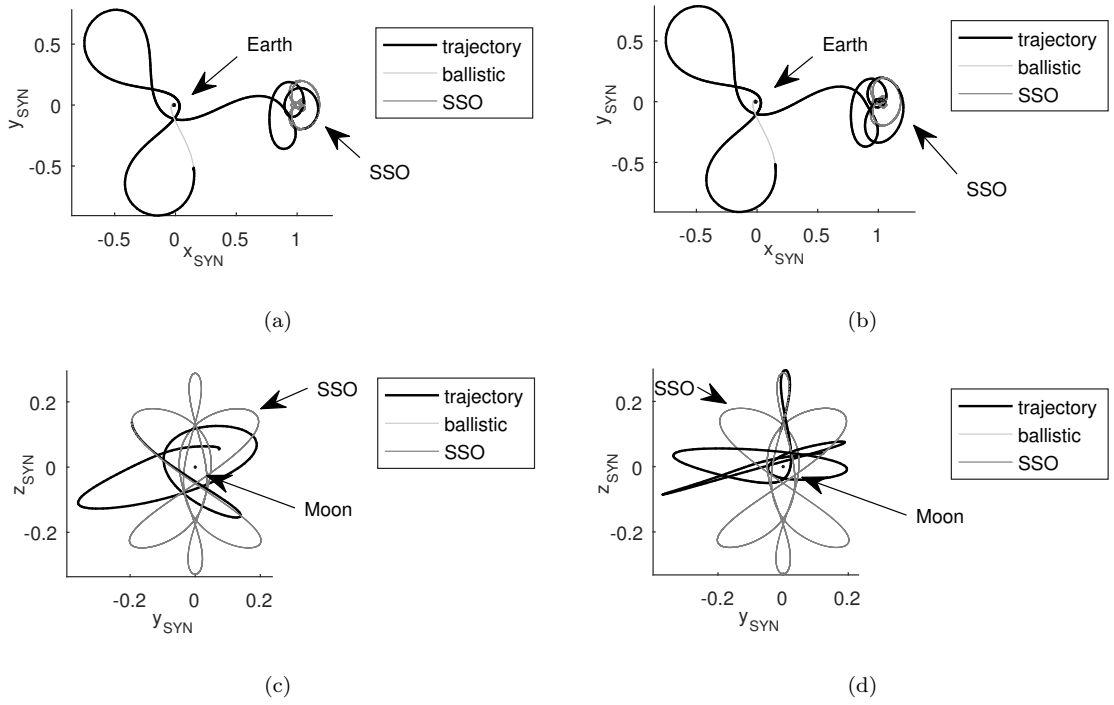

Fig. 17 (a) Trajectory for SC1 projected on $(\hat{\mathbf{x}}_{SYN}, \hat{\mathbf{y}}_{SYN})$-plane. (b) Trajectory for SC2 projected on $(\hat{\mathbf{x}}_{SYN}, \hat{\mathbf{y}}_{SYN})$-plane. (c) Trajectory detail for SC1 projected on $(\hat{\mathbf{x}}_{SYN}, \hat{\mathbf{y}}_{SYN})$-plane. (d) Trajectory detail for SC2 projected on $(\hat{\mathbf{x}}_{SYN}, \hat{\mathbf{y}}_{SYN})$-plane.

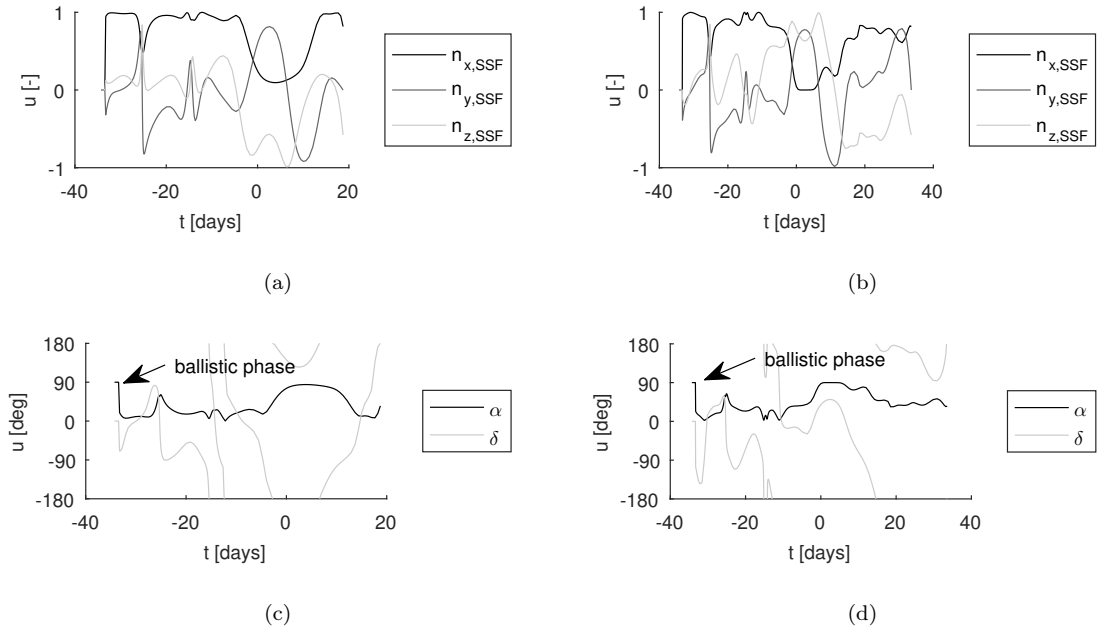

Fig. 18 (a) Control for SC1, expressed in Cartesian coordinates. (b) Control for SC2, expressed in Cartesian coordinates. (c) Control for SC1, expressed in cone and clock angle. (d) Control for SC2, expressed in cone and clock angle

C. Active rotation rate constraint

In order to address the singularities in the control, the same trajectories are regenerated but with an active rotation rate constraint. These results are shown in Fig. 19.

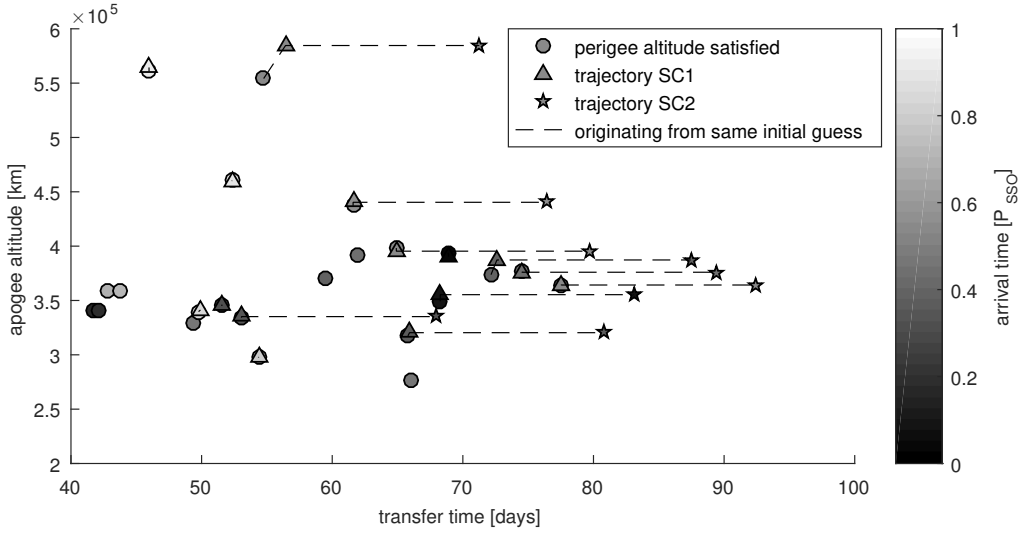

Fig. 19 Results with rotation rate constraint active.

By comparing Fig. 16 and 19, it can be seen that similar transfer times are found, irrespective of the activation of the maximum rotation rate constraint. However, the average apogee altitude is increased, indicating that constraining the rotation rate results in less energy efficient trajectories. This is expected as the locally optimal steering law requires high rotation rates and thus constraining the rotation rate results in a less optimal control. Furthermore, by enforcing a maximum rotation rate, the constraint violation is increased, requiring more iterations in the Gauss-Newton algorithm with respect to the unconstrained case. These iterations will cause the control profile to diverge from the initial guess, which can cause either an increase or decrease in performance. As the results are feasible and not optimal, a direct comparison of the performance between Fig. 16 and 19 cannot be made. However, the results do show that multiple feasible solar-sail trajectories continue to exists while including a maximum rotation rate constraint of 20 deg/day.

Out of 160 initial guesses, 23 trajectories are found with a perigee altitude of 250 km, of which the quickest trajectory achieves a transfer in 41.8 days. For this trajectory however, no matching trajectory for SC2 was found. Instead, out of 9 found trajectories for SC2, the quickest result

completes the transfer in 67.89 days, while a trajectory for SC1 with identical departure conditions completes its transfer in 53.06 days. These trajectories are shown in Fig. 20 with respect to the SYN frame, where the corresponding control as a function of time is given in Fig. 21. In order to determine the departure conditions, a value of $\phi_{2,0} = 135.4$ deg has been assumed in Eq. 17.

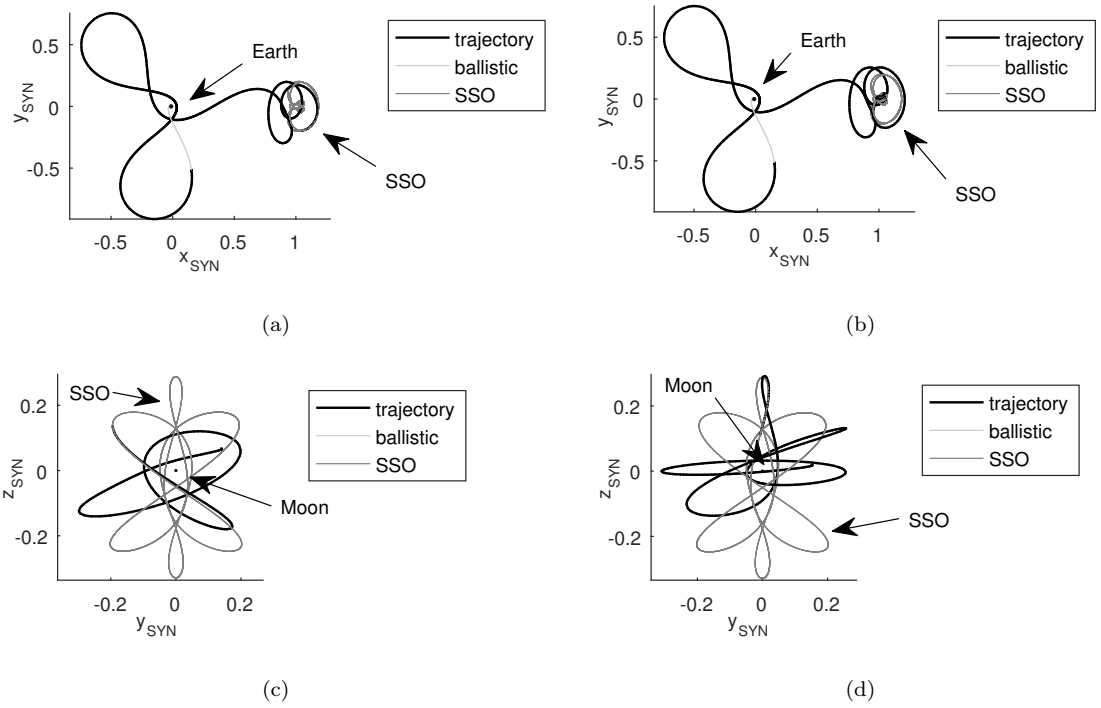

Fig. 20 (a) Trajectory for SC1 projected on $(\hat{\mathbf{x}}_{SYN}, \hat{\mathbf{y}}_{SYN})$-plane. (b) Trajectory for SC2 projected on $(\hat{\mathbf{x}}_{SYN}, \hat{\mathbf{y}}_{SYN})$-plane. (c) Trajectory detail for SC1 projected on $(\hat{\mathbf{x}}_{SYN}, \hat{\mathbf{y}}_{SYN})$-plane. (d) Trajectory detail for SC2 projected on $(\hat{\mathbf{x}}_{SYN}, \hat{\mathbf{y}}_{SYN})$-plane.

The trajectories shown in Fig. 17 and 20 have a similar shape as they are both derived from the same initial guess. Major differences can be seen in Fig. 21, as the maximum rotation rate constraint requires a smooth control profile. Note that δ is undefined for $\alpha = 0$, which allows for rapid change in δ without violating the rotation rate constraint. These results show that solar-sail transfer trajectories are feasible in the Earth-Moon system without requiring long transfer times, low-altitude flybys or singularities in the control.

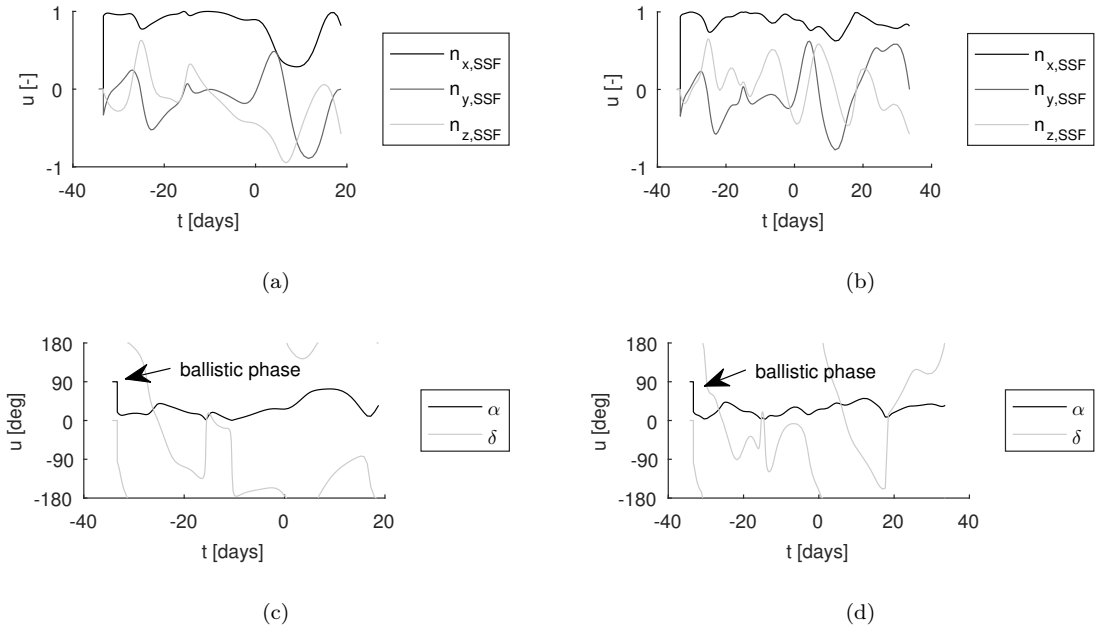

Fig. 21 (a) Control for SC1, expressed in Cartesian coordinates. (b) Control for SC2, expressed in Cartesian coordinates. (c) Control for SC1, expressed in cone and clock angle. (d) Control for SC2, expressed in cone and clock angle

Table 6 Spacecraft subsystem mass estimations in kg.

Payload	Structure	Thermal	Power	TT&C	ADCS	Sail	Total
2.01	1.56	0.26	2.34	0.35	0.51	2.97	10.00
232.89	181.04	30.60	271.13	40.90	58.65	344.90	1160.00

D. Mass budget analysis

The transfer trajectories in Fig. V A are used for the analysis on the mass budget. Two mass budgets are constructed, one for a large spacecraft utilizing the full Soyuz capacity, and another for a 10-kg cubesat demonstration mission. Based on the HEO apogee altitude of 335 200 km, the Soyuz launcher can deliver two spacecraft of 1160 kg each (see Fig. 5), which is comparable to the solar-sail spacecraft described in Ref. [6]. Table 6 contains the results of the preliminary mass budget. By estimating the required sail size, it is found that the 1160-kg mission requires a solar-sail area of 185.71×185.71 m^2 and allows for a 232.89 kg payload, while the 10-kg cubesat mission requires a sail area of 17.24×17.24 m^2 and allows for a 2.01 kg payload.

IX. Conclusion

The purpose of this work was to find feasible solar-sail transfer trajectories to a constellation proposed in previous work. The constellation consists of two spacecraft placed in solar-sail displaced Earth-Moon L_2 vertical Lyapunov orbits and can provide continuous coverage of the Aitken basin and the lunar South Pole, while maintaining a permanent view of the Earth.

The transfer trajectories, opposed to previous Earth-Moon solar-sail trajectory designs in the literature, do not contain singularities in the control history and depart from standard Soyuz Earth parking orbits. The 12^{th}-order Gauss-Labotto collocation method and an adaptive mesh refinement method are applied to rewrite the trajectory problem to a nonlinear programming problem, which is consequently solved using the Gauss-Newton algorithm. It is shown that eight path constraints, such as altitude, rotation rate and continuity constraints, can conveniently be implemented through the application of the collocation method.

The collocation method is used to find sets of two feasible trajectories with identical launch conditions, that can be used to transfer both spacecraft simultaneously to their correctly-phased positions along the solar-sail displaced L_2 vertical Lyapunov orbits. During the transfers, the minimum altitudes with respect to Earth and the Moon are constrained to 10 000 km and four lunar radii, respectively. Also, the maximum rotation rate of the solar sail is constrained to 20 deg/day, which mitigates undesirable control singularities. The quickest transfer time solution shows that the first spacecraft will reach its target orbit after a transfer time of 53.06 days, while the second spacecraft requires a transfer time of 67.89 days. A single Soyuz launch can deliver two 1160-kg spacecraft into these transfer trajectories. A subsystem mass estimation based on reference satellites shows that the spacecraft can carry a 232.89-kg payload and require a solar-sail area of 185.71×185.71 m^2. Similarly, a 10-kg cubesat mission would be able to carry a 2.01-kg payload and requires a 17.24×17.24 m^2 solar sail. These results show that solar-sail transfer trajectories in the Earth-Moon system are feasible without requiring long transfer times, low-altitude flybys or singularities in the control.

References

[1] McInnes, C., *Solar Sailing: Technology, Dynamics and Mission Applications*, Springer-Verlag, Berlin, Germany, 2nd ed., 2004.

[2] Ceriotti, M. and McInnes, C. R., "Generation of Optimal Trajectories for Earth Hybrid Pole Sitters," *Journal of Guidance, Control, and Dynamics*, Vol. 34, No. 3, 2011, pp. 847–859, doi:10.2514/1.50935.

[3] Macdonald, M., McInnes, C., Alexander, D., and Sandman, A., "GeoSail: Exploring the magnetosphere using a low-cost solar sail," *Acta Astronautica*, Vol. 59, No. 8-11, 2006, pp. 757–767, doi:10.1016/j.actaastro.2005.07.023.

[4] Heiligers, J., Parker, J. S., and Macdonald, M., "Novel Solar-Sail Mission Concepts for High-Latitude Earth and Lunar Observation," *Journal of Guidance, Control, and Dynamics*, Vol. 41, No. 1, 2018, pp. 212–230, doi:10.2514/1.g002919.

[5] Ozimek, M. T., Grebow, D. J., and Howell, K. C., "Design of Solar Sail Trajectories with Applications to Lunar South Pole Coverage," *Journal of Guidance, Control, and Dynamics*, Vol. 32, No. 6, 2009, pp. 1884–1897, doi:10.2514/1.41963.

[6] Heiligers, J., van den Oever, T., Ceriotti, M., Mulligan, P., and McInnes, C., "Continuous Planetary Polar Observation from Hybrid Pole-Sitters at Venus, Earth, and Mars," in "The Fourth International Symposium on Solar Sailing," Kyoto, Japan, 2017.

[7] Heiligers, M. V. . J., "Time-Optimal Solar Sail Heteroclinic Connections for an Earth-Mars Cycler," in "Proceedings of the 68th International Astronautical Congress 2017: Unlocking Imagination, Fostering Innovation and Strengthening Security," , 2017.

[8] Macdonald, M. and McInnes, C., "A Near-Term Roadmap for Solar Sailing," in "55th International Astronautical Congress of the International Astronautical Federation, the International Academy of Astronautics, and the International Institute of Space Law," American Institute of Aeronautics and Astronautics, Vancouver, British Columbia, Canada, 2004, doi:10.2514/6.iac-04-u.1.09.

[9] Crawford, I., Anand, M., Cockell, C., Falcke, H., Green, D., Jaumann, R., and Wieczorek, M., "Back to the Moon: The scientific rationale for resuming lunar surface exploration," *Planetary and Space Science*, Vol. 74, No. 1, 2012, pp. 3–14, doi:10.1016/j.pss.2012.06.002.

[10] Coverstone, V. L. and Prussing, J. E., "Technique for Escape from Geosynchronous Transfer Orbit Using a Solar Sail," *Journal of Guidance, Control, and Dynamics*, Vol. 26, No. 4, 2003, pp. 628–634, doi:10.2514/2.5091.

[11] Mengali, G. and Quarta, A. A., "Non-Keplerian orbits for electric sails," *Celestial Mechanics and Dynamical Astronomy*, Vol. 105, No. 1-3, 2009, pp. 179–195, doi:10.1007/s10569-009-9200-y.

[12] Dachwald, B., Mengali, G., Quarta, A. A., and Macdonald, M., "Parametric Model and Optimal Control of Solar Sails with Optical Degradation," *Journal of Guidance, Control, and Dynamics*, Vol. 29, No. 5, 2006, pp. 1170–1178, doi:10.2514/1.20313.

[13] Das-Stuart, A. and Howel, K., "Solar Sail Transfers from Earth to the Lunar Vicinity in the Circular Restricted Problem," in "AIAA/AAS Astrodynamics Specialist Conference," Vail, CO, USA, 2015.

[14] Herman, A., *Improved Collocation Methods with Application to Direct Trajectory Optimization*, Ph.D. thesis, University of Illinous at Urbana-Champaign, 1995.

[15] Herman, J. F., *Improved Collocation Methods to Optimize Low-Thrust, Low-Energy Transfers in the Earth-Moon System*, Ph.D. thesis, University of Colorado at Boulder, 2015.

[16] Betts, J. T., "A Survey of Numerical Methods for Trajectory Optimization," *Journal of Guidance, Control, and Dynamics*, Vol. 21, No. 2, 1998, pp. 193–207, doi:10.2514/2.4231.

[17] de Boor, C., "Good Approximation by Splines with Variable Knots," in "Spline Functions and Approximation Theory," BirkhÃď user Basel, Vol. 363, pp. 57–72, 1973, doi:10.1007/978-3-0348-5979-0_3.

[18] Bjorck, Å., *Numerical Methods for Least Squares Problems*, Society for Industrial and Applied Mathematics, 1996, doi:10.1137/1.9781611971484.

[19] Perez, E., *Soyuz user's manual*, Arianespace, 2nd ed., 2012.

[20] Williams, D., "Planetary Fact Sheet - Metric," Online, 2015.

[21] Chobotov, V., *Orbital Mechanics*, AIAA, 3rd ed., 2002.

[22] Bate, R., Mueller, D., and White, J., *Fundamentals of Astrodynamics*, Dover Publications, New York, USA, 1st ed., 1971.

[23] Herman, A. L. and Conway, B. A., "Direct optimization using collocation based on high-order Gauss-Lobatto quadrature rules," *Journal of Guidance, Control, and Dynamics*, Vol. 19, No. 3, 1996, pp.

592–599,
doi:10.2514/3.21662.

[24] Martins, J. R. R. A., Sturdza, P., and Alonso, J. J., "The complex-step derivative approximation," *ACM Transactions on Mathematical Software*, Vol. 29, No. 3, 2003, pp. 245–262, doi:10.1145/838250.838251.

[25] Davis, T. A., *UMFPACK User Guide*, SuiteSparse, 5th ed., 2016.

[26] Russell, R. D. and Christiansen, J., "Adaptive Mesh Selection Strategies for Solving Boundary Value Problems," *SIAM Journal on Numerical Analysis*, Vol. 15, No. 1, 1978, pp. 59–80, doi:10.1137/0715004.

[27] Shampine, L. F. and Reichelt, M. W., "The MATLAB ODE Suite," *SIAM Journal on Scientific Computing*, Vol. 18, No. 1, 1997, pp. 1–22, doi:10.1137/s1064827594276424.

[28] Wertz, J., *Space Mission Analysis and Design*, Space Technology Library, Microcosm press/Kluwer Academic Publishers, El Segundo, California, USA, 3rd ed., 1999.

[29] Dachwald, B., "Optimal Solar Sail Trajectories for Missions to the Outer Solar System," *Journal of Guidance, Control, and Dynamics*, Vol. 28, No. 6, 2005, pp. 1187–1193, doi:10.2514/1.13301.

[30] Mengali, G. and Quarta, A. A., "Near-Optimal Solar-Sail Orbit-Raising from Low Earth Orbit," *Journal of Spacecraft and Rockets*, Vol. 42, No. 5, 2005, pp. 954–958, doi:10.2514/1.14184.

[31] Eldad, O., Lightsey, E. G., and Claudel, C., "Minimum-Time Attitude Control of Deformable Solar Sails with Model Uncertainty," *Journal of Spacecraft and Rockets*, Vol. 54, No. 4, 2017, pp. 863–870, doi:10.2514/1.a33713.

3

Conclusions and Recommendations

This chapter presents the conclusions of the research work carried out during this thesis. In section 3.1 the research questions are answered, followed by proposed recommendations in section 3.2. Finally, the implications of the results with respect to the development of space exploration in general are evaluated in section 3.3.

3.1. Conclusions

The research objective of this thesis is to contribute to the development of solar-sail missions, by designing transfer trajectories to the constellation of solar-sail displaced L_2 vertical Lyapunov orbits in the Earth-Moon system, to support communication with the far side of the Moon as well as the lunar South Pole. The found transfer trajectories, opposed to previous designs if transfers to orbits in the Earth-Moon system, are connected to standard Soyuz highly elliptical parking orbits and do not contain singularities in the control history. The 12^{th}-order Gauss-Labotto collocation method and an adaptive mesh refinement method are applied to rewrite the trajectory problem to a nonlinear programming problem. Search directions are sought using the Gauss-Newton algorithm, while a line search method is applied to find a new estimation of the decision vector. It is shown that eight path constraints, such as altitude, solar-sail rotation rate and continuity constraints, can conveniently be implemented through the application of the collocation method.

The research objective is achieved by answering the main research question and evaluating the research subquestions:

What are the achievable transfer times and spacecraft masses for a solar-sail trajectory from an Earth-based parking orbit to a constellation of solar-sail displaced L_2 vertical Lyapunov orbits in the Earth-Moon system?

a) What transfer time can be achieved by solving the trajectory problem through the application of locally optimal steering laws?

   In total, 2000 trajectories have been generated through the reverse-time integration of the locally optimal steering law. The 2000 trajectories originate from equally spaced initial conditions along the solar-sail displaced L_2 vertical Lyapunov orbit, providing a complete set of all possible transfer trajectories using this steering law. It is shown that some trajectories arrive from outside the Earth-Moon system through the L_2 point while other trajectories crash on the Moon. However, most trajectories contain spiral trajectories around Earth. The highly elliptical spiral trajectories depart from a highly elliptical orbit and have a short transfer time, with a minimum of 50.7 days. The more circularized spiral trajectories contain transfer times longer than a year and depart from medium Earth orbits. It is shown that transfer trajectories are found, but the results contain singularities in the attitude control and do not connect to actual parking orbits.

b) What transfer times can be achieved through the application of the 12^{th}-order Gauss-Lobatto collocation method?

The results generated under research subquestion a) require long transfer times and do not comply with all constraints. In order to improve the quality of the results, the trajectories have been further constrained in the 12^{th}-order Gauss-Lobatto collocation method. The transfer time of the trajectories is reduced by truncating the trajectory close to geostationary orbit altitude. Boundary constraints are subsequently enforced, such that the departure point of the trajectory coincides with a parking orbit with a perigee altitude of 250 km. Path constraints are enforced containing a minimum altitude of 10 000 km with respect to Earth and four lunar radii with respect to the Moon. Then, transfer times are achievable starting from 39.6 days. The obtained trajectories have a higher feasibility than the results found using the locally optimal steering law, due to the elimination of low-altitude flybys. Furthermore, the achievable transfer time has been reduced by 11.1 days.

c) What is the effect on the found transfer trajectories if the maximum solar-sail rotation rate is constrained to 20 deg/day?

The results found under research subquestion b) still contained singularities in the control. A more realistic control profile is found by constraining the maximum rotation rate of the sail to 20 deg/day. The fastest trajectory with a constrained rotation rate achieves a transfer within 41.8 days. The rotation rate constraint causes a larger initial constraint violation, requiring more iterations to solve the trajectory problem. The increase in iterations leads to a solution which is further located from the initial guess, which can cause a decrease or increase in transfer time. As the trajectories are not optimized, the decrease in performance due to the constraint cannot be estimated by a direct comparison. However, it can be concluded that feasible transfer trajectories continue to exist after constraining the maximum rotation rate, with an increase in transfer time of 2.2 days.

d) What is the performance of the found transfer trajectories in terms of spacecraft mass for a realistic mission scenario involving a single Soyuz launch?

The trajectories found under research subquestion c) are further constrained to coincide with Soyuz parking orbits, by enforcing inclination and argument of perigee constraints on the initial condition of the transfer. Trajectories are found for both spacecraft, with identical departure conditions, such that the entire constellation can be initiated using a single Soyuz launch. The fastest set of trajectories achieves a transfer time of 53.1 days for the first spacecraft, while the transfer for the second spacecraft takes 67.9 days. These trajectories depart from a highly elliptical orbit with an apogee altitude of 335 200 km, to which the Soyuz launcher can deliver two 1160-kg spacecraft. A preliminary subsystem analysis shows that the spacecraft requires a sail area of 185.7×185.7 m^2 and can carry a payload mass of 232.9 kg. For a hypothetical 10-kg cubesat spacecraft, a sail area of 17.24×17.24 m^2 is required and a payload mass of 2.01 kg will be available.

From the answers to the research questions it is clear that the objective of this thesis has been achieved as the combined answers to the research sub questions resolve the main research question. The results show that solar-sail transfer trajectories are feasible in the Earth-Moon system without requiring long transfer times, low-altitude flybys or singularities in the control.

3.2. Recommendations

Several recommendations are proposed for further research on solar-sail trajectory design. First of all, some of the assumptions need to be eliminated, resulting in a more accurate dynamical model. Secondly, chosen threshold values used in the constraints formulation can be varied in order to investigate their influence on the performance of the trajectories. Finally, the used collocation method and trajectory transcription can be expanded for future trajectory optimization.

- Expand the dynamical model

The dynamical model adopted in this thesis uses the framework of the circular restricted three-body problem, which assumes circular orbits for the Earth and Moon. In addition, it has been assumed that the Earth-Moon system progresses along a circular orbit around the Sun and that all orbits of the Sun-Earth-Moon system are coplanar in the ecliptic plane. However, in fact, the lunar orbit has an eccentricity of 0.0549 [18], the inclination of the Earth-Moon system with

respect to the ecliptic is 6.68 deg [18] and Earth's orbit around the Sun has an eccentricity of 0.0167 [18]. In order to improve the accuracy of the dynamical model, the elliptical restricted three-body problem can be used to model the Earth-Moon system, inclined to the ecliptic plane, as has already been considered for the orbits of the constellation [8]. Furthermore, as the position of the Sun is already known with respect to the Earth-Moon system, the solar gravity perturbation and the varying solar radiation pressure inside the Earth-Moon system can be included as well. Finally, a detailed trajectory design requires a model utilizing the actual ephemeris of the planets and the Moon, such as DE421 [19].

- Expand the solar-sail model

  In this thesis, the ideal solar-sail model has been adopted to model the acceleration originating from the solar radiation pressure. The ideal solar-sail model assumes that every encountered photon will be reflected specularly. In fact, a realistic solar sail will absorb part of the photons, diffusely reflect part of the solar radiation and will also degrade over time [20]. Due to the thin structure of the sail, deformations and buckling will occur, causing a further reduction in the generated acceleration [1]. When taking these deficiencies into account by employing a non-ideal sail model, the feasibility of the transfer trajectories can be further improved.

- Relax the altitude constraints

  In the results of this thesis, minimum altitude constraints are active to reduce possible gravity gradient perturbations and drag on the solar sails. A rather conservative altitude of 10 000 km is assumed with respect to the Earth and a value of four lunar radii with respect to the Moon. In fact, faster and more efficient transfer trajectories might be possible if low-altitude flybys are allowed. In order to relax the altitude constraints, a detailed analysis is required on solar-sail drag and gravitational perturbations. Note that, at low-altitude flybys, the dynamics change faster, requiring more nodes and mesh refinements in order to accurately model the trajectory.

- Elaborate on the rotation rate constraint

  In this thesis, a constraint is applied enforcing a maximum rotation rate of the solar sail. The assumed value for the maximum rotation rate can be further investigated by analyzing sail attitude dynamics. In practice, not only the maximum rotation rate, but also the maximum angular acceleration will be a limiting factor for attitude control. When rotating the normal direction of a spinning solar sail, nutation and precession can occur [21]. Finally, during detailed mission design, both the attitude and orbital dynamics need to be coupled and solved for simultaneously.

- Construct a detailed mass budget

  The current mass budget is constructed using reference data for communication satellites. Incorporating a solar sail will influence the design of the satellite structure, the attitude control system and the propulsion subsystem. Since only a limited number of solar-sail missions have been carried out to date, an accurate estimation using reference spacecraft cannot be made and thus a detailed spacecraft mass budget needs to be defined.

- Include a variable time vector

  In this work, the time vector that describes the time at the nodes of the discretized transfer is described as a constant vector and remains constant during iterations of the transfer trajectory. By varying the fixed departure and arrival time of the transfer trajectory, the radius of convergence can be increased leading to more transfer trajectories. Furthermore, a variable time vector can later be optimized using optimization algorithms.

- Expand the collocation method with an optimization technique.

  The posed problem in this thesis has been solved using a robust and efficient collocation method. Equality and inequality constraints are conveniently implemented without the need for an active-set strategy. This leads to feasible trajectories that do not require low-altitude flybys or singularities in the control. Although the found trajectories are feasible, the trajectories have not been optimized for a specific mission objective. By combining the collocation method with an optimization technique, optimal trajectories may be found subjected to the imposed constraints, with shorter transfer times or higher payload masses.

3.3. Implications

In addition to the conclusions, which answer the technical research questions, the contributions by this thesis to space exploration on a more higher level are discussed in this section.

First, the presented method in this thesis is applied to design transfer trajectories to solar-sail displaced L_2 vertical Lyapunov orbits in the Earth-Moon system. However, the application of the developed method is not limited to solar-sail displaced L_2 vertical Lyapunov orbits. Instead, the method can be applied to other trajectory problems, by replacing the selected target orbit in the Earth-Moon system. This way, the method can be applied to find transfers departing from a parking orbit around Earth to the clover-shaped constellation in Ref. [22], the lunar pole-sitter mission in Ref. [12] or other solar-sail orbits in the Earth-Moon system. The dynamical system can also be altered, by replacing the used set of ordinary differential equations. If the Sun-Earth circular restricted three body problem is included, the method can be used to find transfers to the so called quasi-pole-sitters in Ref. [7], without the need for any propellant consumption. The method may also be applied to find transfers between the North pole-sitter and South pole-sitter orbits, providing a propellant-free alternative to the work in Ref. [6].

Second, the solar-sail transfer trajectories are designed using minimum altitude as well as maximum rotation rate constraints. Opposed to previous results [12, 13], no singularities in the controls are present, resulting in feasible solar-sail transfer trajectories within the Earth-Moon system. This demonstrates that the 12^{th}-order Gauss-Lobatto collocation method can be applied to highly constrained problems. Furthermore, by considering both the control, $\mathbf{u}$, as well as the derivative of the control, $\dot{\mathbf{u}}$, as decision variables, it was possible to constrain the solar-sail rotation rate. The representation of the control can be applied to other solar-sail problems as well, leading to an increased feasibility of the design of future solar-sail orbits and trajectories.

Finally, the design of the transfer trajectories is required for future solar-sail missions, such as the proposed constellation. By designing the transfer trajectory, the transfer times as well as possible spacecraft mass are found, addressing a gap in literature. The designed trajectories also show the applicability of solar-sail transfers in the Earth-Moon system, advocating for solar-sail technology as an propellant-free alternative to low-thrust propulsion systems.

Appendices

A

Appendix: Verification and Validation

This appendix contains the results of the verification and validation procedures which have been conducted to support the credibility of the results. First, it is verified that the individual building blocks are correctly implemented with respect to the conceptual model. Secondly, it is validated that the model output resembles feasible solutions to the trajectory problem.

A.1. Verification

In order to do verify the implementation of the solar-sail acceleration, the so-called solar-sail acceleration ”bubble” is reconstructed [1]. Furthermore, the implementation of the overall dynamics is verified by reintegrating the solar-sail displaced L_2 vertical Lyapunov orbit.

A.1.1. Verification of the solar-sail acceleration bubble

For a perfect solar sail, the solar-sail acceleration acts along the solar-sail normal vector. By varying the controls, such as the cone or clock angle, the direction and magnitude of the acceleration vector changes. To verify the implementation of the acceleration model, the acceleration bubble from Ref. [1] is reconstructed, by varying the cone angle, α, over a range from 0 deg to 90 deg for a clock angle of both 0 deg and 180 deg. The resulting acceleration bubble is shown in Fig. A.1. It can be seen that the shape of the acceleration bubble agrees with the reference solution in Ref. [1]. Also, the maximum acceleration corresponds to the value of $a_{0,EM} = 0.1$ as considered in this thesis.

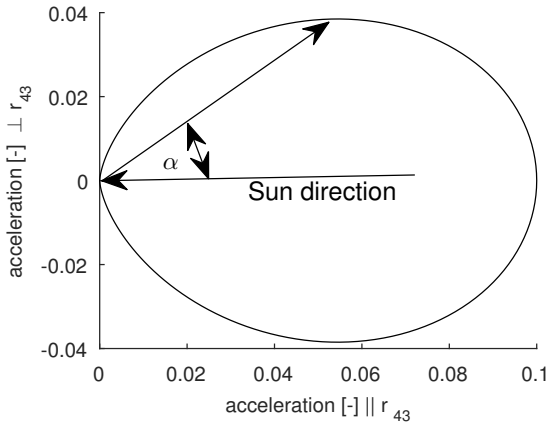

Figure A.1: Solar-sail acceleration for varying sail attitudes. Acceleration given in dimensionless units for the Earth-Moon system. Vector $\mathbf{r_{43}}$ is the sails position vector with respect to the Sun.

A.1.2. Verification of the dynamical model

The dynamical model used in Ref. [8] is identical to the dynamical model used in this thesis, the solar-sail augmented Earth-Moon circular restricted three body problem. In order to verify that the dynamical model has been correctly implemented, the solar-sail displaced L_2 vertical Lyapunov orbit from Ref. [22] is reconstructed. For each point along the integrated orbit, the position error with respect to the reference solution provided by the authors of Ref. [22] is evaluated, where the result is shown in Fig. A.2. It can be seen that the integration error after one period equals only 7.59 m, and thus the dynamical model is assumed to be verified.

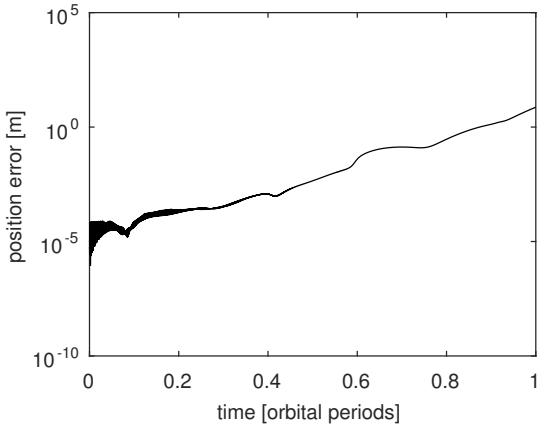

Figure A.2: Position error of integrated solution with respect to the reference solution from Ref. [8] for one period of the solar-sail displaced L_2 vertical Lyapunov orbit.

A.2. Validation

First, it is validated that the used dynamics represent the actual accelerations in the Earth-Moon system. Secondly, the initial guess generator is validated by reconstructing results from Ref. [13]. Furthermore, the accuracy of the input and output of the collocation method are validated by reintegrating trajectories and determining the constraint violation. Finally, the mesh of a found trajectory is compared to the mesh of MATLAB®'s "ode45.m" function [23], validating that the error is equidistributed along the segments.

A.2.1. Validation of the dynamical model

The correct implementation of the dynamical model was verified by reintegrating the solar-sail displaced L_2 vertical Lyapunov orbit in section A.1.2. It is assumed that the used approximations of the dynamical model including the circular restricted three-body problem, solar-sail attitude model and planar Sun model are sufficiently validated by Ref. [8] and [12]. Based on this assumption, no validation is required in which the approximations in the dynamical model will be compared with respect to the actual dynamics of a solar sail in the Earth-Moon problem.

A.2.2. Validation of the initial guess generator

In this thesis, the locally optimal steering law is applied to generate initial guesses for the collocation method. In order to validate the output of the initial guess generator, the results from Ref. [13] are reproduced. Transfer trajectories are generated departing from geostationary transfer orbit (GTO) to an L_1 Lyapunov orbit in the Earth-Moon system. The specific Lyapunov orbit has a period of approximately 12 days and a Jacobi value of 3.1630. The transfers are generated using reverse time propagations, similar to the approach in this thesis. An $a_{0,EM}$ value of 0.5 mm/s^2 is assumed as well as the ideal sail model. The planar Sun model is replaced by a model where the Sun is inclined with respect to the Earth-Moon system. The trajectories travel along the stable manifold of the Lyapunov orbit for approximately 18 days, before arriving at the L_1 Lyapunov orbit. In order to limit the eccentricity of the found transfer trajectories, the solar sail is feathered at regions around apogee. The found trajectory can be seen in an inertial frame in Fig. A.3(a), where Fig. A.3(b) contains the reference solution. The inertial $\hat{\mathbf{x}}_{\mathbf{IRF}}$-axis coincides with the synodic $\hat{\mathbf{x}}_{\mathbf{SYN}}$-axis of the Earth-Moon system at $t = 0$, where $t = 0$

is chosen as the arrival time of the spacecraft on the stable manifold. Furthermore, the altitude as a function of time can be seen in Fig. A.3(c), which should be compared to the altitude of the reference solution in Fig. A.3(d).

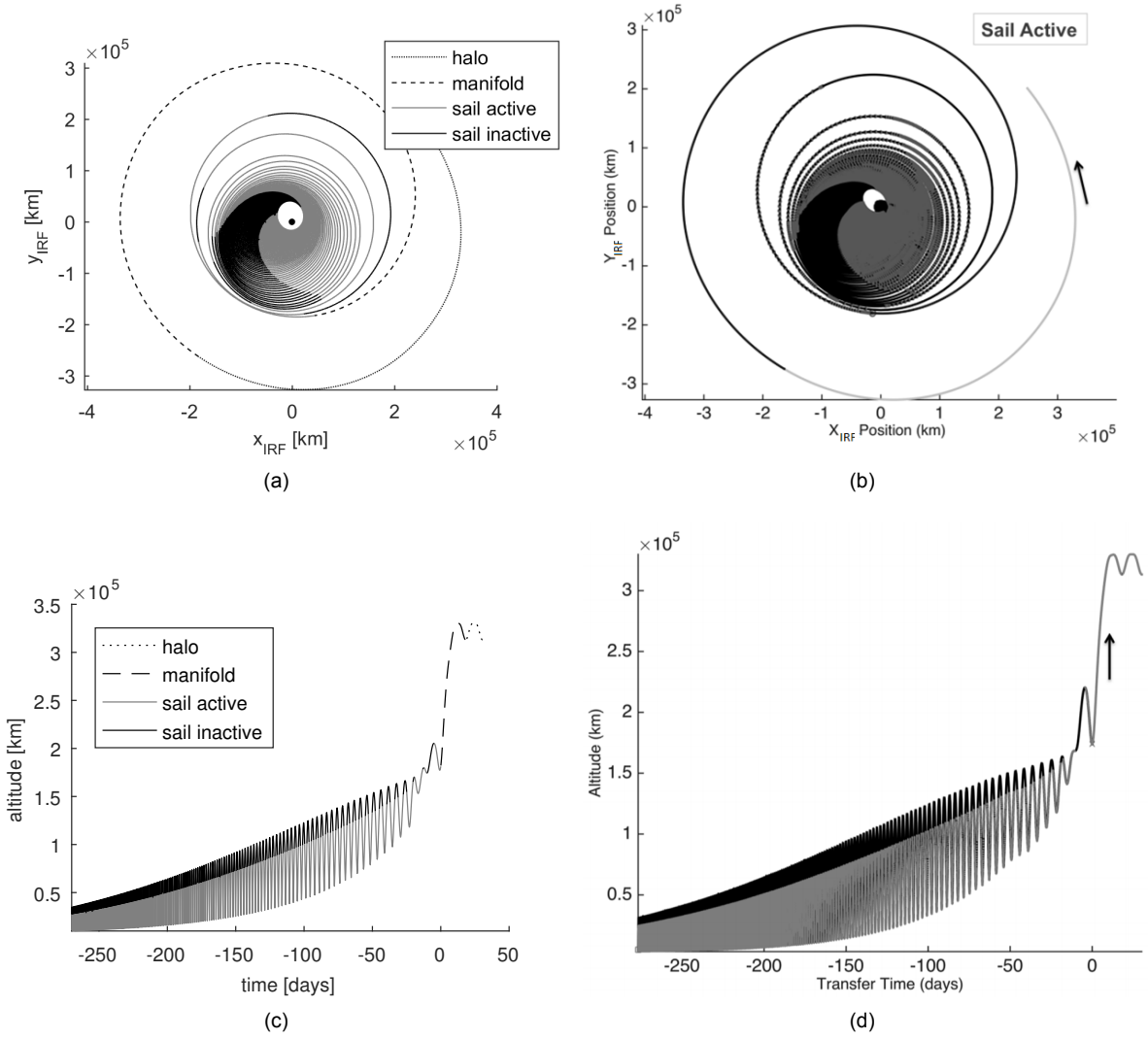

Figure A.3: Figures contain a transfer trajectory found using the locally optimal steering law. (a) Trajectory in an inertial reference frame. (b) Reference trajectory in an inertial reference frame, image taken from Ref. [13]. (c) Altitude of trajectory plotted against time. (d) Altitude of reference trajectory plotted against time, image taken from Ref. [13].

Some small discrepancies can be seen, which can be attributed to the following issues. First of all, the exact geometry of the L_1 Lyapunov orbit is not given. Secondly, the exact arrival time on the L_1 Lyapunov orbit and travel time along the stable manifold are rounded off to full days. Finally, the size and definition of the constrained region around apogee is unknown. Small changes in the initial conditions, or definition of the constrained region around apogee, cause major changes in the trajectory geometry. It is assumed that all of these discrepancies, are not caused by the implementation of the locally optimal steering law or the initial guess generator, but rather by the definition of the initial conditions. From the similarities in geometry and transfer time in Fig. A.3(a) to A.3(d), it can be assumed that the initial guess generator indeed produces the desirable transfer trajectories and is thus correctly implemented.

A.2.3. Validation of collocation method input and output

The initial guesses produced in this thesis are much shorter than the results in Fig. A.3(b). In order to validate that the input for the collocation method contains a near-feasible trajectory, the initial guess, transcripted to collocation nodes, is reintegrated in MATLAB®'s "ode45.m" function [23]. After the collo-

cation method converges, it should also be validated that the collocation method output complies with the dynamics as well as the constraints. The results for both the input and output are shown in Fig. A.4(a) to A.4(f).

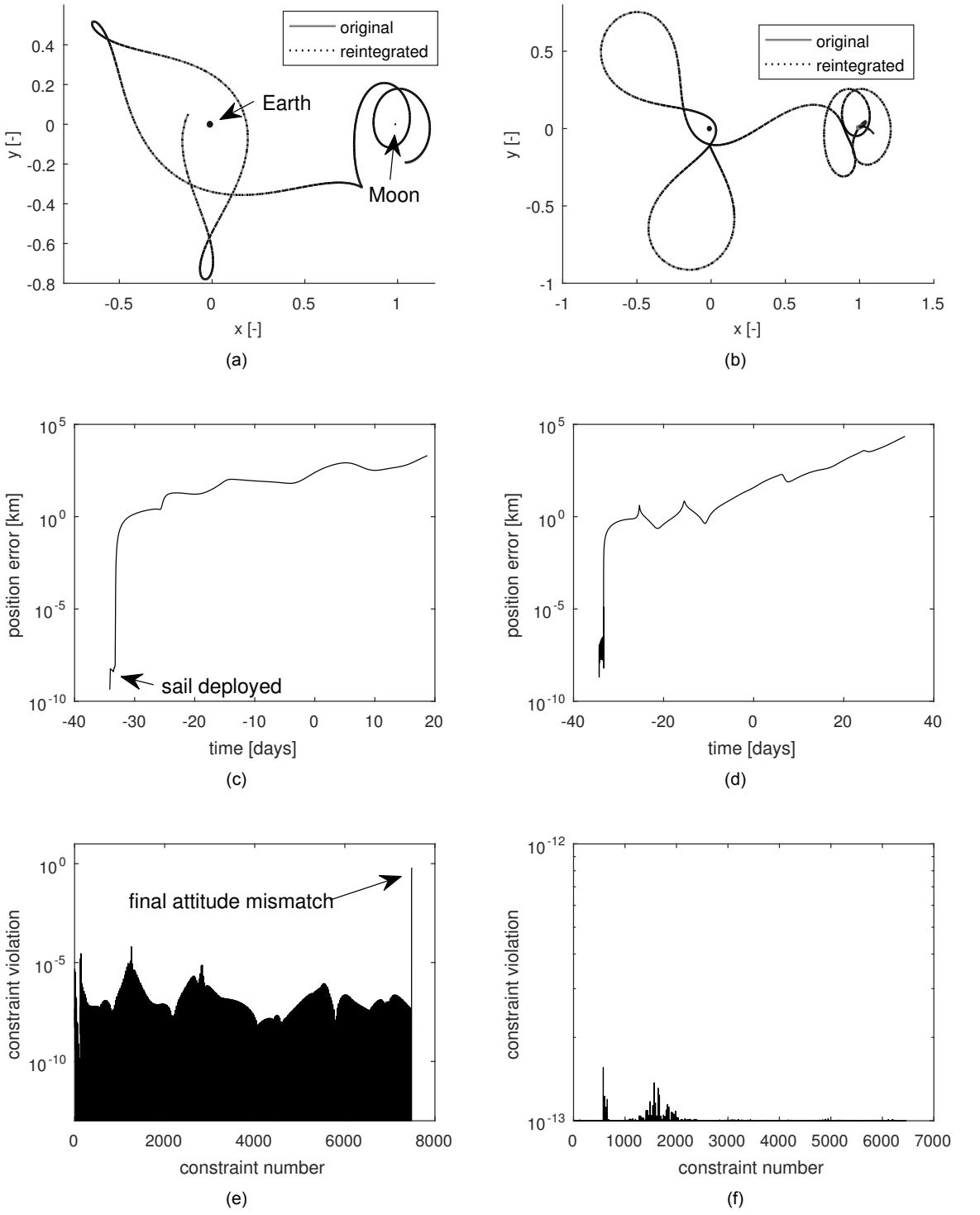

Figure A.4: (a) Trajectory of the initial guess versus the reintegrated dynamics. (b) Trajectory found using the collocation method versus the reintegrated dynamics. (c) Position error of the initial guess versus the reintegrated dynamics. (d) Position error of the output of the collocation method versus the reintegrated dynamics. (e) Constraint violation of the initial guess. (f) Constraint violation of the output of the collocation method.

The reintegrated trajectories are shown in Fig. A.4(a) and A.4(b). The general shape of the initial guess trajectory is preserved even when integrating for periods longer than a month. The same is true for the converged trajectory, although the trajectory starts to diverge after the final flyby near the Moon.

The position error along the integrated trajectory is shown in Fig. A.4(c) and A.4(d). The position error after completing the 40-day trajectory of the initial guess is equal to 2033 km, while the converged trajectory has a total integration error of 22 800 km. Note that the accumulated error for the position grows significantly during the first and second flyby, causing a larger error for the converged solution than for the initial guess. The position error shows a small dip at high altitudes due to smaller velocities.

The constraint violation of the initial guess is shown in Fig. A.4(e). A large constraint violation exists at the moment of sail deployment, due to the non-continuity of the dynamics between two nodes. This problem is addressed during the numerous mesh refinement iterations, where the non-continuity of the dynamics is placed exactly on the node points. The maximum error is below 10^{-4}, except for the segment on which the solar sail deploys and the final node, where the locally optimal attitude profile creates an offset with respect to the required attitude for the solar-sail orbit. The model solves the trajectory problem according to the imposed constraints. In Fig. A.4(f), it can be seen that the constraint violation is significantly reduced for the output of the the collocation method, with the maximum error being lower than 10^{-12}.

A.2.4. Validation of the mesh refinements

In this thesis, the collocation method is applied using an mesh refinement technique based on Ref. [12, 24], which attempts to equidistribute the error over each segment. The found mesh within the collocation technique is compared to the mesh distribution when reintegrating the solution using MATLAB®'s "ode45.m" function [23], see Fig. A.5.

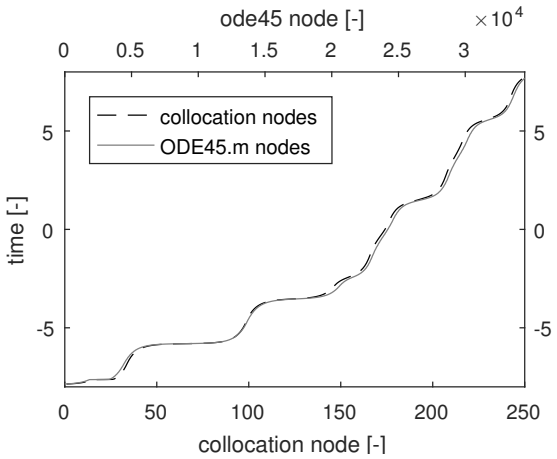

Figure A.5: Mesh distribution of both the collocation algorithm and MATLAB®'s "ode45.m" function [23]. Time is given in dimensionless units for the Earth-Moon system.

In Fig. A.5 can be seen that the mesh distribution of the collocation method approximates the mesh distribution of MATLAB®'s "ode45.m" function. Concentrations of nodes are placed at flybys, while fewer nodes are used when the spacecraft is further removed from either the Earth or Moon. Using the results from MATLAB®'s "ode45.m" function as a reference solution, it can be assumed that error is successfully equidistributed, validating the mesh refinement technique.

Bibliography

[1] McInnes, C. *Solar Sailing: Technology, Dynamics and Mission Applications*. Springer-Verlag, Berlin, Germany, 2nd ed., 2004.

[2] van der Ha, J., Mimasu, Y., Tsuda, Y. and Mori, O. "Solar and Thermal Radiation Models and Flight Evaluation for IKAROS Solar Sail." *Journal of Spacecraft and Rockets*, vol. 52(3):pages 958–967, may 2015. doi:10.2514/1.a33158.

[3] Katan, C. "NASA's Next Solar Sail: Lessons Learned from Nanosail-D2." In "26th Annual AIAA/USU Conference on Small Satellites," North Logan, UT, USA, 2012.

[4] Ridenoure, R. W., Spencer, D. A., Stetson, D. A., Betts, B., Munakata, R., Wong, S. D., Diaz, A., Plante, B., Foley, J. D. and Bellardo, J. M. "Status of the Dual CubeSat LightSail Program." In "AIAA SPACE 2015 Conference and Exposition," American Institute of Aeronautics and Astronautics, aug 2015. doi:10.2514/6.2015-4424.

[5] Macdonald, M. and McInnes, C. "A Near-Term Roadmap for Solar Sailing." In "55th International Astronautical Congress of the International Astronautical Federation, the International Academy of Astronautics, and the International Institute of Space Law," American Institute of Aeronautics and Astronautics, Vancouver, British Columbia, Canada, oct 2004. doi:10.2514/6.iac-04-u.1.09.

[6] Ceriotti, M. and McInnes, C. R. "Generation of Optimal Trajectories for Earth Hybrid Pole Sitters." *Journal of Guidance, Control, and Dynamics*, vol. 34(3):pages 847–859, may 2011. doi:10.2514/1.50935.

[7] Heiligers, J., van den Oever, T., Ceriotti, M., Mulligan, P. and McInnes, C. "Continuous Planetary Polar Observation from Hybrid Pole-Sitters at Venus, Earth, and Mars." In "The Fourth International Symposium on Solar Sailing," Kyoto, Japan, Jan. 2017.

[8] Heiligers, J., Parker, J. S. and Macdonald, M. "Novel Solar-Sail Mission Concepts for High-Latitude Earth and Lunar Observation." *Journal of Guidance, Control, and Dynamics*, vol. 41(1):pages 212–230, jan 2018. doi:10.2514/1.g002919.

[9] Crawford, I., Anand, M., Cockell, C., Falcke, H., Green, D., Jaumann, R. and Wieczorek, M. "Back to the Moon: The scientific rationale for resuming lunar surface exploration." *Planetary and Space Science*, vol. 74(1):pages 3–14, dec 2012. doi:10.1016/j.pss.2012.06.002.

[10] Farquhar, R. W. "The Utilization of Halo Orbits in Advanced Lunar Operations." Tech. rep., NASA TN D-6365, 1971.

[11] Grebow, D. J., Ozimek, M. T., Howell, K. C. and Folta, D. C. "Multibody Orbit Architectures for Lunar South Pole Coverage." *Journal of Spacecraft and Rockets*, vol. 45(2):pages 344–358, mar 2008. doi:10.2514/1.28738.

[12] Ozimek, M. T., Grebow, D. J. and Howell, K. C. "Design of Solar Sail Trajectories with Applications to Lunar South Pole Coverage." *Journal of Guidance, Control, and Dynamics*, vol. 32(6):pages 1884–1897, nov 2009. doi:10.2514/1.41963.

[13] Das-Stuart, A. and Howel, K. "Solar Sail Transfers from Earth to the Lunar Vicinity in the Circular Restricted Problem." In "AIAA/AAS Astrodynamics Specialist Conference," Vail, CO, USA, aug 2015.

[14] Perez, E. *Soyuz user's manual*. Arianespace, 2 ed., mar 2012.

[15] Walmsley, M., Heiligers, J., Ceriotti, M. and McInnes, C. “Optimal Trajectories for Planetary Pole-Sitter Missions.” *Journal of Guidance, Control, and Dynamics*, vol. 39(10):pages 2461–2468, oct 2016. doi:10.2514/1.g000465.

[16] Betts, J. T. “A Survey of Numerical Methods for Trajectory Optimization.” *Journal of Guidance, Control, and Dynamics*, vol. 21(2):pages 193–207, mar 1998. doi:10.2514/2.4231.

[17] Ozimek, M. T. and Howell, K. C. “Low-Thrust Transfers in the Earth-Moon System, Including Applications to Libration Point Orbits.” *Journal of Guidance, Control, and Dynamics*, vol. 33(2):pages 533–549, mar 2010. doi:10.2514/1.43179.

[18] Williams, D. “Planetary Fact Sheet - Metric.” Online, nov 2015. URL `http://nssdc.gsfc.nasa.gov/planetary/factsheet/`.

[19] Folkner, W., Williams, J. and Boggs, D. “The Planetary and Lunar Ephemeris DE 421.” Tech. rep., NASA JPL, 2009. URL `http://ipnpr.jpl.nasa.gov/progress_report/42-178/178C.pdf`.

[20] Dachwald, B., Mengali, G., Quarta, A. A. and Macdonald, M. “Parametric Model and Optimal Control of Solar Sails with Optical Degradation.” *Journal of Guidance, Control, and Dynamics*, vol. 29(5):pages 1170–1178, sep 2006. doi:10.2514/1.20313.

[21] Wie, B. *Space Vehicle Dynamics and Control*. AIAA Education Series Textbook, 2008.

[22] Heiligers, J., Macdonald, M. and Parker, J. S. “Extension of Earth-Moon libration point orbits with solar sail propulsion.” *Astrophysics and Space Science*, vol. 361(7), jun 2016. doi:10.1007/s10509-016-2783-3.

[23] Shampine, L. F. and Reichelt, M. W. “The MATLAB ODE Suite.” *SIAM Journal on Scientific Computing*, vol. 18(1):pages 1–22, jan 1997. doi:10.1137/s1064827594276424.

[24] de Boor, C. “Good Approximation by Splines with Variable Knots.” In “Spline Functions and Approximation Theory,” vol. 363, pages 57–72. Birkhäuser Basel, 1973. doi:10.1007/978-3-0348-5979-0_3.

.


TU Delft